https://doi.org/10.5194/gmd-2023-152
Preprint. Discussion started: 30 August 2023


Geoscientific Model Development Discussions
Open Access

# To quantify the impact of SST feedback periodicity on atmospheric intraseasonal variability in the tropical regions

Yung-Yao Lan[1], Huang-Hsiung Hsu[1] and Wan-Ling Tseng[2]

[1]Research Center for Environmental Changes, Academia Sinica, Taipei 11529, Taiwan

[2]International Degree Program in Climate Change and Sustainable Development, National Taiwan University,Taipei 10617, Taiwan

*Correspondence to*: Huang-Hsiung Hsu (hhhsu@gate.sinica.edu.tw)

https://doi.org/10.5194/gmd-2023-152
Preprint. Discussion started: 30 August 2023


Geoscientific Model Development Discussions

**Abstract**

This study couples a high-resolution 1-D TKE ocean model (the SIT model) with the Community Atmosphere Model 5.3 (CAM5.3; hereafter CAM5–SIT) configuration, to highlight significant experiments that investigate the influence of different periods of sea surface temperature (SST) feedback, such as 30 minutes, 1, 3, 6, 12, 18, and 30 days, on the Madden-Julian Oscillation (MJO). It substantially breaks through the limitations of flux coupler through air–sea coupling. The aim is to assess the scientific reproducibility and consistency of the findings across different SST feedback cycles in the field of modeling science. Comparing the results to the fifth generation ECMWF reanalysis (ERA5), the high-frequency experiments (C–CTL, C–1day, and C–3days) and low-frequency experiments (C–6days, C–12days, and C–18days) exhibit higher fidelity in capturing various aspects of MJO, except for the C–30days experiment. These aspects in characterizing the basic features of the MJO such as encompass intraseasonal periodicity, eastward propagation, coherence in the MJO band, tilting vertical structure, the lead–lag relationship between MJO-related atmosphere and SST variation, phase 2 column-integrated moisture static energy (MSE) tendency, and the projection of all MSE terms onto the MSE tendency of ERA5 across the Maritime Continent (MC). The MJO simulation performance of this study can be assessed in two ways. Firstly, the high-frequency experiments generally capture MJO characteristics, albeit with slightly lower results compared to ERA5 and NOAA data. Secondly, the low-frequency experiments show robust MJO simulations, which can be attributed to the accumulation of energy (temperature) in the upper ocean. This leads to the accumulation of shortwave and longwave radiations, as well as surface heat fluxes from the atmosphere.

https://doi.org/10.5194/gmd-2023-152
Preprint. Discussion started: 30 August 2023




## 1. Introduction

The Madden–Julian Oscillation (MJO) is a large-scale tropical circulation that propagates eastward from the tropical Indian Ocean (IO) to the western Pacific (WP) with a periodicity of 30–80 days (Madden and Julian, 1972). In the Indo-Pacific region, there is increasing evidence that MJO processes are involved in intraseasonal variability of sea surface temperature (SST) (Chang et al., 2019; DeMott et al., 2014, 2015; Jiang et al., 2015, 2020; Krishnamurti et al., 1998; Li et al., 2014; Li et al., 2020a; Newman et al., 2009; Pei et al., 2018; Stan, 2018; Tseng et al., 2015). These studies confirm that including air–sea interactions significantly improves the simulation of the MJO.

The ocean's response to intraseasonal atmospheric variability, such as surface shortwave radiation, turbulent heat fluxes controlled by wind speed, and ocean processes driven by wind stress, plays a crucial role in causing intraseasonal SST variability related to the MJO (Li et al., 2014). Incorporating two-way coupling between the ocean and atmosphere is expected to be valuable for simulating and predicting intraseasonal variability (e.g., DeMott et al., 2014; Lan et al., 2022; Stan, 2018; Tseng et al., 2015, 2020). However, the influence of sub-seasonal (e.g., beyond a phase) air–sea coupling on convection and related oceanic features is still not fully understood.

In this study, we aim to investigate the specific effects of oceanic feedback frequency (FF) in sub-seasonal periodicity through air–sea coupling on the eastward propagation of the MJO as simulated by the Community Atmosphere Model 5.3 (CAM5.3) coupled with the one-column ocean model Snow–Ice–Thermocline (SIT), referred to as CAM5–SIT (Lan et al., 2022). The tropical air–sea interaction, influenced by the upper ocean, plays a crucial role in determining MJO characteristics

https://doi.org/10.5194/gmd-2023-152
Preprint. Discussion started: 30 August 2023




due to the high heat capacity of the upper ocean, which acts as a significant source of heat energy for atmospheric variability (Liang and Du, 2022). The SIT model, consisting of 41 vertical layers, enables the simulation of SST and upper-ocean temperature variations with high vertical resolution. The vertical resolution is set to 12 layers within the first 10.5 m and 6 layers between 10.5 m and 107.8 m. The fine resolution simulates the upper ocean warm layer, which includes a layer at 0.05 mm that replicates the cool skin of the ocean surface (Tseng et al., 2015, 2020; Lan et al., 2010, 2022). Previous studies have emphasized the importance of vertical resolution in accurately simulating the MJO, with Tseng et al. (2015) demonstrating the necessity of a 1 m vertical resolution when coupling SIT with the European Centre/Hamburg Model version 5 (ECHAM5), referred to as ECHAM5–SIT in the tropics. Furthermore, Shinoda et al. (2021) indicated the positive impact of high vertical resolution near the ocean surface on MJO prediction abilities based on simulations of the National Oceanic and Atmosphere Administration (NOAA) Climate Forecast System. Ge et al. (2017) highlighted the presence of a high vertical temperature gradient within the upper 10 m of the MJO event, particularly during dry and clear periods, underscoring the need for a resolution of approximately 1 m to accurately capture intraseasonal SST variability.

Several recent studies have made significant progress in understanding the impact of air–sea coupling on the MJO, particularly at sub-daily scales (e.g., DeMott et al., 2015; Kim et al., 2018; Seo et al., 2014; Voldoire et al., 2022; Zhao and Nasuno, 2020). However, there is relatively limited discussion on air–sea coupling at the sub-seasonal scale. Several studies have undertaken investigations into the impact of intraseasonal SST on the MJO by conducting various model experiments, encompassing both coupled and uncoupled models. (e.g., DeMott et al., 2014; Gao et al., 2020b; Klingaman, and Demott, 2020; Pariyar et al., 2023; Stan, 2018). Stan

https://doi.org/10.5194/gmd-2023-152
Preprint. Discussion started: 30 August 2023

Geoscientific Model Development
Discussions
Open Access

(2018) found that in the air–sea coupling run, the peak in surface fluxes (latent heat and sensible heat) is stronger and occurs earlier compared to the uncoupling run with sub-5-day SST variability. Additionally, the absence of 1–5-day variability in SST promotes the amplification of westward power associated with Rossby waves. Based on these modeling studies, it is concluded that the atmospheric response to sub-seasonal SST variances can be determined. Replay simulations using time-varying coupled global climate model (CGCM) SSTs as atmospheric general circulation model (AGCM) boundary conditions showed a reduced dynamic range of SST anomalies, leading to weakened air–sea heat fluxes and eastward propagation (DeMott et al., 2014; Gao et al., 2020b; Klingaman, and Demott, 2020; Pariyar et al., 2023). Stan (2018) also demonstrated that eliminating 1–5-day variability of surface boundary forcing reduces the intraseasonal variability of the tropics during boreal winter in the case of CGCM SSTs as AGCM boundary conditions. However, the effect of sub-seasonal SST variances on the MJO is still not fully understood in both coupled and uncoupled experiments.

As demonstrated by Fu et al. (2017), underestimation (overestimation) of the air–sea coupling's impact on MJO simulations occurs when there is weakness (strong) in the intraseasonal SST anomaly. Understanding the manifestation of heat fluxes in the significant intraseasonal oscillation (ISO) is crucial for the development of intraseasonal SST variability (Liang et al., 2018). In aquaplanet simulations conducted by Arnold et al. (2013), where equatorial SST were set at approximately 26°, 29°, 32°, and 35° C, it was observed that the intraseasonal variance (wavenumbers 1–3, periods 20–100 days) exhibited a significant and consistent increase with increasing SST. Furthermore, Savarin and Chen (2022) have found that improved air–sea heat fluxes result in systematic enhancements in precipitation, winds, SST, and the mixed layer in the ocean. Hence, the combination of higher

https://doi.org/10.5194/gmd-2023-152
Preprint. Discussion started: 30 August 2023



tropical SST and enhanced SST variances collectively contribute to an intensified eastward propagation of the MJO.

Improvements in the MJO in coupled simulations can be attributed to several factors. Firstly, enhanced low-level convergence and convective instability to the east of convection, as well as enhanced latent heat fluxes and SST cooling to the west of convection, contribute to the improved eastward propagation and regulation of MJO periodicity (DeMott et al., 2014). SST gradients have been found to induce patterns of mass convergence and divergence within the marine boundary layer (MBL), initiating atmospheric convection (de Szoeke and Maloney, 2020; Lambaerts et al., 2020). The basic state SST or basic state moist static energy (MSE) plays a crucial role in MJO instability (Wang et al., 2016). Moisture convergence in the MBL accumulates MSE and increases convective instability to the east of the main convection, facilitating the eastward propagation of the MJO (Hsu and Li, 2012; Wang et al., 2016). The increased low-level convergence is associated with shallow convection induced by SST-induced convective instability (DeMott et al., 2014). An analysis of MSE convergence by de Szoeke and Maloney (2020) demonstrates that intraseasonal SST fluctuations drive the overall MSE tendency, contributing to MJO generation and propagation. Arnold et al. (2013) demonstrate that the vertical advection projection exhibits a positive trend. Specifically, they find that it acts as a strong damping mechanism at low SST, whereas it transitions into an energy source at high SST. Based on this observation, we can infer that alterations in vertical MSE advection are probably accountable for the amplified variability of the MJO in relation to SST.

The structure of this paper is organized as follows. Section 2 introduces the models, data, methodologies, and experiments employed in this study. The performance of the CAM5–SIT models in simulating the MJO is discussed in Section 3, while Section 4 focuses on the impact of different sub-seasonal periodicity

https://doi.org/10.5194/gmd-2023-152
Preprint. Discussion started: 30 August 2023



configurations on MJO simulations through detailed MJO diagnostics. Finally, Section 5 presents the conclusions drawn from this study.

## 2. Data, model experiments, and methodology

### 2.1 Observational, atmospheric, and oceanic data

An observational data set used in this study includes precipitation from the Global Precipitation Climatology Project (GPCP, 1° resolution, 1997–2010; Adler et al., 2003), outgoing longwave radiation (OLR, 1° resolution, 1997–2010; Liebmann, 1996), and daily SST (optimum interpolated SST, OISST, 0.25° resolution, 1989–2010; Banzon et al., 2014) from the National Oceanic and Atmosphere Administration.

The atmospheric variables used in this study were obtained from the fifth-generation reanalysis of the European Centre for Medium-Range Weather Forecasts (ECMWF) known as the fifth generation ECMWF reanalysis (ERA5), with a resolution of 0.25° for the period of 1989–2020 (Hersbach and Dee, 2016). Various variables from ERA5 were considered, including zonal wind, meridional wind, vertical velocity, temperature, specific humidity, sea level pressure, geopotential height, latent heat, sensible heat, and shortwave and longwave radiation. For the initial conditions of a SIT model, SST data was obtained from the Hadley Centre Sea Ice and Sea Surface Temperature dataset version 1 (HadISST1), with a resolution of 1° for the period of 1982–2001 (Rayner et al., 2003). The ocean subsurface data, including climatological ocean temperature, salinity, and currents in 40 layers, were retrieved from the National Centers for Environmental Prediction (NCEP) Global Ocean Data Assimilation System (GODAS) with a resolution of 0.5° for the period of 1980–2012 (Behringer and Xue, 2004). These data were used for nudging in the SIT model.

https://doi.org/10.5194/gmd-2023-152
Preprint. Discussion started: 30 August 2023


Geoscientific Model Development Discussions

## 2.2 Experimental design

In this study, we investigate the role of oceanic FF in sub-seasonal periodicity using the coupled model CAM5–SIT and the uncoupled AGCM (A–CTL). Previous studies (Lan et al., 2022; Tseng et al., 2022) have provided a detailed description of the every timestep coupling CAM5–SIT model and its performance in simulating atmospheric variability and the MJO. This study involved a series of 30-year numerical experiments (as shown in Table 1). We overcame the limitations of the National Center for Atmospheric Research (NCAR) Climate System Model (CSM) Flux Coupler (CPL) by implementing similarly asymmetric exchange frequencies between the atmosphere and the ocean. The SST value is fixed at each timestep within the experimental periodicity through a straightforward approach to create various intraseasonal SST (e.g., 30 minutes, 1, 3, 6, 12, 18, and 30 days) feedback atmospheric experiments. It is important to note that every timestep involves bidirectional interaction in the CPL.

Two sets of experiments were conducted, each representing a different SST feedback frequency:

(1) The high-frequency SST feedback set: This set includes the control experiment (C–CTL) with SST feedback at every timestep (FF as 48/day), as well as experiments with SST feedback once a day (C–1day: FF as 1/day) and every 3 days (C–3days: FF as 1/3days), respectively.

(2) The low-frequency SST feedback set: This set includes experiments with SST feedback returning to the atmosphere every 6 days (C–6days: FF as 1/6days), 12 days (C–12days: FF as 1/12days), 18 days (C–18days: FF as 1/18days), and 30 days (C–30days: FF as 1/30days), respectively.

In all experiments, there is a common configuration: CAM5 forces SIT at each

https://doi.org/10.5194/gmd-2023-152
Preprint. Discussion started: 30 August 2023



timestep, SIT has the same vertical resolution, and coupling is implemented between 30° N to 30° S in the entire tropics. The only difference lies in the frequency of SIT's SST feedback into the atmosphere. This choice is driven by two factors related to tropical coupling.

Firstly, the MJO predominantly occurs in tropical regions (Jiang et al., 2020; Kang et al., 2020; Shinoda et al., 2021), hence coupling was specifically implemented between 30° N to 30° S. This focuses the coupling on the region where the MJO is most active.

Secondly, coupling a one-dimensional ocean model without surface flux correction to the extratropics would neglect the influence of strong ocean currents, such as the Kuroshio and Gulf Streams, leading to significant biases. Therefore, coupling is limited to the tropical region to avoid these biases and ensure a more realistic representation of the air–sea interactions relevant to the MJO.

Forcing of the coupled and uncoupled models' initial conditions was done using a climatological monthly-mean HadSST1 dataset. The monthly Global Ocean Data Assimilation System (GODAS) dataset was linearly interpolated to obtain daily values of oceanic temperature, salinity, u-current, and v-current for nudging purposes. The ocean was weakly nudged (using a 30-day time scale) between depths of 10.5 m and 107.8 m, and strongly nudged (using a 1-day time scale) below 107.8 m, based on the climatological ocean temperature data from NCEP GODAS. No nudging was applied in the upper-most 10.5 meters.

During the simulation, the SIT recalculated the SST within the tropical air–sea coupling region, which spans from 30° S to 30° N. Outside this coupling region, the prescribed annual cycle of HadSST1 was used. The ocean bathymetry for the SIT was derived from the NOAA ETOPO1 data (Amante and Eakins, 2009). To ensure consistency and comparability, all observational, atmospheric, oceanic, and reanalysis

https://doi.org/10.5194/gmd-2023-152
Preprint. Discussion started: 30 August 2023



data were interpolated into a horizontal resolution of 1.9° × 2.5° for model initialization, nudging, and comparison of experimental simulations.

### 2.3 Methodology

The analysis focused primarily on the boreal winter period (November–April), which exhibits the most pronounced eastward propagation of the MJO. To identify intraseasonal variability, the CLIVAR MJO Working Group diagnostics package (CLIVAR, 2009) and a 20–100-day filter (Wang et al., 2014) were employed. MJO phases were defined following the index (namely, RMM1 and RMM2) proposed by Wheeler and Hendon (2004), which utilizes the first two principal components of combined near-equatorial OLR and zonal winds at 850 and 200 hPa. The band-pass filtered data were employed to calculate the index and define the MJO phases.

Furthermore, an analysis of column-integrated MSE budgets was conducted to investigate the association between the tropical convection and large-scale circulations. The column-integrated MSE budget equation (e.g., Sobel et al., 2014) is approximately given by

$$\langle\frac{\partial h}{\partial t}\rangle' = -\langle u\frac{\partial h}{\partial x}\rangle' - \langle v\frac{\partial h}{\partial y}\rangle' - \langle w\frac{\partial h}{\partial p}\rangle' + \langle LW\rangle' + \langle SW\rangle' + \langle SH\rangle' + \langle LH\rangle' \quad (1)$$

where *h* denotes the moist static energy;

$$h = c_pT + gz + L_vq \quad (2)$$

where $T$ is temperature (K); $q$ is specific humidity (Kg Kg$^{-1}$); $c_p$ is dry air heat capacity at constant pressure (1004 J K$^{-1}$ kg$^{-1}$); $L_v$ is latent heat of condensation (taken constant at 2.5 × 10$^6$ J kg$^{-1}$); $u$ and v are horizontal and meridional velocities (m s$^{-1}$), respectively; $\omega$ is the vertical pressure velocity (Pa s$^{-1}$); *LW* and *SW* are the longwave and shortwave radiation fluxes (W m$^{-2}$), respectively; and *LH* and *SH* are the latent and sensible surface heat fluxes (W m$^{-2}$), respectively. The angle brackets

https://doi.org/10.5194/gmd-2023-152
Preprint. Discussion started: 30 August 2023



($\langle * \rangle$) represent mass-weighted vertical integration from 1000 to 100 hPa; and the intraseasonal anomalies are represented as $\langle * \rangle'$, which were isolated using a 20–100-day bandpass filter (Wang et al., 2014).

## 3. Results

### 3.1 The basic state SST variability

The variability of SSTs plays a crucial role in the dynamics of the MJO. In the absence of interseasonal SST variability, as observed in the uncoupled A–CTL simulations, the eastward propagation of the MJO is disrupted, resulting in weakened or fragmented MJO activity. Studies based on observations from TOGA COARE and DYNAMO have revealed that MJO events exhibit a stronger ocean temperature response compared to average conditions (de Szoeke et al., 2014). Interseasonal SST variability in the tropics, resulting from air–sea coupling, significantly impacts the behavior of the MJO behavior and atmospheric circulation. Warmer SSTs to the east of convection enhance the release of latent heat, triggering atmospheric convection and strengthening the MJO. Conversely, cooler SSTs in this region create a more stable atmospheric environment, which is less favorable for the development and propagation of the MJO (DeMott et al., 2015). The activity and strength of the MJO are influenced by SST in the region. Cooler than average sea surface temperatures (SSTs) in this region are associated with the passage of MJO activity and a tendency towards decreased intensity.

Table 2 presents the oceanic temperature anomalies for the DJF seasonal mean, including the differences in oceanic temperature between the SST and depths of 10m ($\overline{\Delta \boldsymbol{T}}_{\boldsymbol{0-10m}}$) and 30m ($\overline{\Delta \boldsymbol{T}}_{\boldsymbol{0-30m}}$), as well as phase anomalies of 20–100 days maximum and minimum SST and oceanic temperature at 10m depth ($T_{10m}$). The region of 110–130° E and 5–15° S was selected because it shows the largest variation in the 20–100-day bandpass-filtered SST when the MJO passes over the Indo-Pacific region. Except

https://doi.org/10.5194/gmd-2023-152
Preprint. Discussion started: 30 August 2023



for C–30days, the DJF seasonal mean SST shows a slight increase with the higher SST feedback periodicity, while the SST standard deviation remains within 0.8 K. In the critical region (110–130° E, 5–15° S), experiments with high frequency SST feedback periodicity exhibit a mean SST of less than 1.4 K during DJF, while experiments with low frequency SST feedback periodicity range from -1.0 K to 0.5 K compared to the OISST dataset.

Understanding the variations in SST during DJF in the Indo-Pacific region is critical for predicting and interpreting the MJO's behavior. The temperature differences between observed monthly mean SST and NCEP GODAS reanalysis data ($\overline{\Delta \boldsymbol{T}}_{\mathbf{0-10m}}$ and $\overline{\Delta \boldsymbol{T}}_{\mathbf{0-30m}}$) as well as AGCM are not compared here. The $\overline{\Delta \boldsymbol{T}}_{\mathbf{0-10m}}$ in high-frequency experiments maintain 0.1K temperature difference. In low-frequency experiments, $\overline{\Delta \boldsymbol{T}}_{\mathbf{0-10m}}$ increase from 0.1 to 1.0 K as SST feedback periodicity increases correspondingly. The temperature difference ($\overline{\Delta \boldsymbol{T}}_{\mathbf{0-30m}}$) in both high-frequency and low-frequency experiments remains approximately 0.8K, except for C–30days. In the daily OISST SST phase anomalies, the maximum and minimum values are approximately maintained at $\pm$0.2K. However, compared to OISST or model simulations, the uncoupled A–CTL, which uses monthly mean OISST, shows significantly smaller mean anomalies in the SST phase, on the order of 1–2 magnitudes smaller. In the high-frequency experiments, SST phase anomalies exhibit similar magnitudes of $\pm$0.2K as observed. The SST means in both the high-frequency and low-frequency experiments reach their maximum in phase 3, lagging about 1 phase behind the OISST. The maximum and minimum $T_{10m}$ values indicate that the atmospheric heat/cooling ocean process is consistently mixed in the C–CTL experiment, but not in the low-frequency experiments.

According to CLIVAR diagnostics, there are diverse behaviors observed in MJO simulations, as indicated by the slight difference between phase anomalies of C–3days

https://doi.org/10.5194/gmd-2023-152
Preprint. Discussion started: 30 August 2023



maximum SST and $T_{10m}$ compared to C–CTL and C–1day, which indicates diverse behaviors of MJO simulations, according to CLIVAR diagnostics. Fu et al. (2017) indicated that too weak intraseasonal SST anomaly in coupled models would lead to the underestimation of the impacts of air–sea coupling on MJO simulations.

## 3.2 MJO simulation: high-frequency and low-frequency SST feedback experiments

### 3.2.1 General structure

We conducted SST feedback experiments with high-frequency and low-frequency responses, as well as uncoupled AGCMs, to compare the simulated characteristics of the MJO. The propagation characteristics of the different experiments were analyzed using the wavenumber-frequency spectrum (W-FS). The spectra of unfiltered U850 in ERA5 reanalysis, A–CTL, C–CTL, C–1day, C–3days, C–6days, C–12days, C–18days, and C–30days are shown in Fig. 1a–i, respectively. The C–CTL experiment accurately captures the eastward propagating signals at zone wavenumber 1 and for periods of 30 to 80 days (Fig. 1a and 1c), although with a slightly larger amplitude than ERA5. However, the uncoupled A–CTL produces an unrealistic spectral shift to time scales longer than 30–80 days (Fig. 1b) and exhibits westward propagation at wavenumber 2.

C–3days tend to reduce the interseasonal variability of the MJO compared to the C–CTL experiment under coupled runs, which is consistent with the results of Stan (2018) in uncoupled experiments that force the atmosphere by surface boundary. de Boisséson et al. (2012) also found that hindcasts of the MJO are sensitive to changes in SST boundary conditions, although daily and weekly SST forecasts are similar. In this study, it was observed that the high-frequency experiments limited the variance of the MJO. According to Stan (2018), the lack of 1–5-day SST variability favors an increase in westward power associated with Rossby waves. The W-FS of the C–1day

https://doi.org/10.5194/gmd-2023-152
Preprint. Discussion started: 30 August 2023



experiment showed two peaks for zone wavenumber 1 over the 30 to 80-day period. This might be attributed to the inconsistency in day and night variations when the SST feedback of C–1day is returned to the atmosphere at different locations. Except for C–30days, the low-frequency experiments enhance the W-FS of U850 during interseasonal periods. In this study, low-frequency SST variability is not enhanced in the unrealistic westward W-FS by increasing SST feedback periodicity until C–18days.

The Hovmöller diagrams in Fig. 2a–i depict the evolution of 10° N–10° S averaged precipitation and U850 anomalies on intraseasonal timescales, represented by lagged correlation coefficients between precipitation averaged over 10° S–5° N, 75–100° E. In GPCP/ERA5, there is observed eastward propagation of precipitation and U850 from the eastern IO to the dateline, with precipitation leading U850 by approximately a quarter of a cycle. The propagation speed of the 30–80-day filtered U850 anomaly is 5 m $s^{-1}$ (Fig. 2a). However, the A–CTL simulations exhibit westward-propagating signals over the IO and weak, slow eastward propagation over the MC and WP (Fig. 2b), which is also reflected in the W-FS shown in Fig. 1b, indicating enhanced westward propagation in wavenumber 2. The Hovmöller diagrams of the high-frequency and low-frequency experiments (Fig. 2c–h) display the key eastward propagation characteristics of both precipitation and U850, as well as the phase relationship between them, except for C–30days. The simulated correlations between precipitation and U850 anomalies in the experiments are generally weaker compared to GPCP and ERA5, particularly when crossing the MC into the WP. Fig. 2b and Fig. 2c–h highlight the contrast, indicating that coupling a 1-D TKE ocean model can significantly enhance an AGCM ability to simulate key characteristics of the MJO, such as amplitude, propagation direction and speed, and the phase relationship between precipitation and circulation. When crossing the MC, the Hovmöller diagram of C–3days precipitation exhibits a substantial weakening compared to other high-frequency and low-frequency experiments (except for C–30days). This weakening is accompanied by a weaker easterly zonal wind in the MC. This finding is consistent with the results from the W-FS in Fig. 1e. Neither precipitation nor U850 exhibit clear eastward propagation characteristics over C–30days. Further detailed discussions on this topic will be presented in the subsequent chapter.

We conducted a cross-spectral analysis to examine the phase lag and coherence between the tropical circulation and convection. Figures 3a–i illustrate the symmetric part of OLR and U850 for NOAA/ERA5 data, A–CTL, C–1day, C–3days, C–6days, C–12days, C–18days, and C–30days, respectively. The MJO band exhibits a high degree of coherence, indicating a strong correlation between NOAA MJO-related OLR signal and wavenumbers 1–3 (Fig. 3a). The simulated phase lag in the 30–80-day band is approximately 90°, consistent with previous studies (Ren et al., 2019; Wheeler and Kiladis 1999). All model experiments show significant coherence within wavenumber 3 in the MJO band, with a phase lag similar to NOAA/ERA5 data. However, A–CTL at wavenumber 1 only exhibits half of the observed coherency peaks, and the coherence at wavenumbers 2–3 for the 30–80-day period is weaker compared to NOAA/ERA5 data. The experiments C–CTL, C–1day, C–3days, C–6days, C–12days, and C–18days exhibit similar coherency peaks to NOAA/ERA5 at wavenumber 1. Additionally, as the SST feedback periodicity increases, the experiments between C–12days and C–30days simulate unrealistic coherency over wavenumber 9 in the MJO band (Fig. 3g–i).

The 20–100-day filtered precipitation anomalies (shaded) and SST anomalies (contour) were averaged over the 10° S–10° N region (Fig. 4a–i). Phase-longitude diagrams were used to analyze the relationship between precipitation and SST

https://doi.org/10.5194/gmd-2023-152
Preprint. Discussion started: 30 August 2023

Geoscientific Model Development Discussions
Open Access

fluctuations and to establish the connection between air–sea coupling and convection. Except for C–30days, both GPCP/OISST and the coupled experiments clearly showed the eastward propagation of enhanced convection with positive SST anomalies (Fig. 4a and 4c–i). The amplitude of SST increases in low-frequency experiments, as indicated in Table 1 and Fig. 4f–h, resulting in precipitation anomalies lagging by approximately 2–3 phases than SST, particularly when crossing the MC. Liang et al. (2018) indicated SST leading precipitation by 10 days implies air–sea interactions at the intraseasonal timescale during MJO events, with SST playing a crucial role in modulating the MJO's intensity and propagation. The A–CTL simulations exhibited weak SST anomalies and stationary precipitation when using the monthly average SST interpolation from OISST. In contrast, the C–30days experiment showed unrealistic SST and precipitation variability. Overall, eastward propagation of the MJO is not favored by either minimal or large SST fluctuations (Fig. 4b and 4i). By comparing the coupled experiments with the aforementioned simulations, it became evident that air–sea interaction plays a crucial role in facilitating eastward propagation. Fu et al. (2017) found that a robust intraseasonal SST anomaly is associated with successive MJO events and supports the propagation of MJOs, as supported by NOAA OLR and TRMM precipitation. This study highlights the significant improvement in eastward propagation simulations achieved by incorporating the air–sea interaction process into the model with distinct high-frequency and low-frequency experiments, even with a simple 1-D ocean model like SIT.

### 3.2.2 Vertical structures of the MJO in the atmosphere

Air–sea interaction plays a significant role in influencing atmospheric moisture and convection associated with the MJO (Savarin and Chen, 2022). During periods of

https://doi.org/10.5194/gmd-2023-152
Preprint. Discussion started: 30 August 2023



convective suppression, the surface air temperature generally tracks the SST closely (de Szoeke et al., 2014). A warmer upper ocean enhances low-level atmospheric convergence, leading to increased low-level moisture and preconditioning that facilitate eastward propagation and deep convection (DeMott et al., 2014). Hovmöller diagrams in Fig. 5a–i illustrate the relationship between air temperature anomalies (contoured, in K) and the vertically tilting structure of specific humidity (shading, in g kg$^{-1}$) from the surface to the upper troposphere (200 hPa) over the 10° S–10° N and 120–150° E regions. Positive air temperature anomalies lead positive specific humidity anomalies by approximately 2–3 phases, with the maximum specific humidity occurring between 700–500 hPa. In ERA5 and the coupled experiments (excluding C–30days), there are two relatively high values of air temperature at 300 and 700 hPa, respectively. However, in A–CTL, the maximum specific humidity anomaly occurs at 700 hPa, and there is a vertically stationary structure in specific humidity anomaly and an opposite tilting in air temperature (Fig. 5b). A–CTL also exhibits a decrease in low-level moisture anomaly due to negative air temperature anomalies below 700 hPa. C–30days, on the other hand, shows an unrealistic vertical tilting structure in both specific humidity and air temperature anomalies (Fig. 5i).

According to the WISHE-moisture mode theory (Fuchs and Raymond, 2017), the combination of mean easterly zonal winds and moisture plays a role in the propagation and destabilization of the MJO. East of the convective MJO, enhanced easterly winds induce atmospheric destabilization and moistening, leading to the propagation of the MJO (Sentić et al., 2020). Figure 6 displays the averaged p-vertical velocity anomaly (OMEGA, Pa s$^{-1}$, shaded) and zonal wind anomaly (m s$^{-1}$, contour, interval 0.5) between phase 3 and phase 4 over the 15° N–15° S region. We specifically selected the phase between 3 and 4 to examine the period leading up to the MJO convection crossing the MC. Prior to the onset of the MJO in this phase,

https://doi.org/10.5194/gmd-2023-152
Preprint. Discussion started: 30 August 2023


Geoscientific Model Development
Discussions

there is typically a buildup of convection over the land areas of the MC, which encompass countries such as Indonesia, Malaysia, and the Philippines. This land convection acts as a precursor to the MJO as it creates favorable conditions and sets the stage for the subsequent development of organized atmospheric disturbances. This can be observed in the low-level ascending OMEGA shown in Figure 6a, specifically between 120–150° E. The land convection over the MC is driven by a combination of factors, including the local geography, land-ocean temperature contrasts, and large-scale atmospheric conditions. The complex topography and the presence of extensive water bodies surrounding the MC provide favorable conditions for the uplift of moist air, which leads to the formation of local convection. Additionally, the temperature differences between the warm ocean waters and the relatively cooler land surfaces contribute to the instability and uplift of air masses.

In C–CTL, there is an enhanced easterly wind anomaly between 120° E and 180° E at 800–600 hPa (Fig. 6c). The stronger easterly winds, coupled with radiative heating, such as net downwelling surface solar radiation, lead to warmer upper ocean temperatures (not shown). This heat stored in the upper ocean influences surface fluxes and drives convection in the atmosphere (de Szoeke et al., 2014; Hsu et al., 2019). In the western IO and MC region (Fig. 6c–h), there is a spatial distribution of negative OMEGA (ascending motion) anomalies during phase 3–4, accompanied by westerly wind anomalies to the west of MJO convection below 500 hPa in the coupled experiments (except C–30days). In A–CTL during phase 3–4, negative OMEGA anomalies are observed both east and unrealistically west of the MC (Fig. 6b). Generally, the low-frequency experiments exhibit stronger negative OMEGA, westerly wind anomalies and land convection compared to the high-frequency experiments, except for C–30days. In the case of C–30days, deep convection in the

https://doi.org/10.5194/gmd-2023-152
Preprint. Discussion started: 30 August 2023



IO, MC, and WP regions is weakened as local convection occurs randomly during phase 3–4 (Fig. 6i).

### 3.2.3 The vertical structure of the ocean responds to the MJO

Understanding the interaction between the atmosphere and upper ocean is essential for studying the MJO, particularly the upper ocean's response to strong atmospheric forcing. Accurate representation of air–sea interactions, including momentum and heat fluxes associated with the MJO, is crucial for capturing the MJO in coupled model simulations, as emphasized by Hong et al. (2017). It is crucial to properly couple an ocean model that incorporates MJO air–sea interaction for a comprehensive understanding. Such coupling can lead to warmer or cooler surface oceans and shallower or deeper mixed layer depths before or after MJO convection in the tropics, resulting from improved vertical resolution in the upper ocean (Tseng et al., 2015; Lan et al., 2022). These oceanic changes, in turn, induce atmospheric responses through the ocean feedback process. In this study, we employ a SIT model coupled with CAM5 to investigate the frequency of air–sea coupling and its impact on MJO simulation. This ocean model incorporates a high vertical resolution that captures important features such as the cool skin layer and diurnal warm layer, as well as the gradient of temperature in the upper ocean. In the OISST, high-frequency, and low-frequency experiments, the strongest phase anomalies of maximum SST occur between phases 2 and 3 (as shown in Table 1), particularly in the region of (110–130 ° E, 5–15° S), where SST variations associated with the MJO are most prominent. Figure 7 illustrates the average oceanic temperature between 0- and 60-meters depth during phase 2–3, filtered for the 20–100-day period, represented by shaded and contour plots with an interval of 0.03 Kelvin. In the high-frequency experiments, the upper oceanic temperatures exhibit warming patterns within 30 meters depth at 100–

https://doi.org/10.5194/gmd-2023-152
Preprint. Discussion started: 30 August 2023

Geoscientific Model Development Discussions

140° E, while cooling is observed near the dateline (as shown in Fig. 7a–c). During phase 2–3, as the MJO convection progresses into the IO (60–90° E), it interacts with the ocean surface, leading to a cooling effect in the upper ocean in the C–CTL experiment (Fig. 7a), which is more pronounced compared to the C–3days experiment (Fig. 7c), characterized by stronger interseasonal MJO variability. In the low-frequency experiments, the spatial distribution of warmer upper ocean temperatures is more extensive than in the high-frequency experiments, spanning from the MC to the WP. Additionally, the vertical temperature gradient in this region is greater in the low-frequency experiments compared to the high-frequency experiments. However, in the Indo-Pacific region, the C–30days experiment exhibits an unrealistic spatial distribution of oceanic temperature anomalies, with small areas of both positive and negative anomalous temperature fluctuations (Fig. 7g).

## 4. Discussion

### 4.1 Empirical Orthogonal Function (EOF) analysis

Empirical orthogonal functions (EOF) analysis helps identify spatial patterns and their associated temporal variations, providing insights into the underlying dynamics and relationships within the dataset. The first EOF mode captures the largest fraction of variance in the data, while subsequent modes capture progressively smaller amounts of variance and represent additional patterns. This study builds upon previous research utilizing uncoupling simulations (e.g., DeMott et al., 2014; Stan, 2018) and investigates the influence of interseasonal SST feedback on the MJO by incorporating real air–sea coupling. Figure 8 illustrates the near-equatorial variance explained by the Real-time Multivariate MJO series 1 (RMM1) and series 2 (RMM2), which represent the combined variance explained by the first two empirical orthogonal functions (EOF1 and EOF2) according to Wheeler and Hendon (2004).

https://doi.org/10.5194/gmd-2023-152
Preprint. Discussion started: 30 August 2023



These RMM1 and RMM2 components have proven useful for estimating and characterizing the MJO and its variability. The coupled experiments, when combined with RMM1 and RMM2, demonstrate improved MJO performance compared to A–CTL, with the exception of C–30days. The extension of interseasonal SST feedback periodicity corresponds to an increase in RMM1+RMM2. Generally, the RMM1+RMM2 percentages are larger for the low-frequency experiments compared to the high-frequency experiments, except for C–30days. Among the high-frequency experiments, C–3days shows a slight degradation in RMM1+RMM2, consistent with the observed MJO-related results such as the W-FS for 850-hPa zonal wind (Fig. 1e), the Hovmöller diagram of precipitation crossing the MC (Fig. 2e), the OLR power spectrum at a zonal wavenumber-frequency wavelength (Fig. 3e), the maximum phase-vertical Hovmöller diagram of 20–100-day specific humidity between 700–500 hPa (Fig. 5e), and the cooling effects in the upper ocean (Fig. 7c). However, C–30days exhibits lower skill in terms of RMM1+RMM2 compared to the other coupled simulations due to the presence of excessive local convection and weak large-scale circulation, which is reflected in the unrealistic spatial distribution of oceanic temperature.

### 4.2 The dynamic lead–lag relationship of intraseasonal variability

The lead–lag relationship refers to a situation where one variable (leading) is cross-correlated with the values of another variable (lagging) in subsequent phases, particularly in the case of SST fluctuations and MJO-related atmospheric variations between phase 1 and 8 within the domain of 110–130° E and 5–15° S (Fig. 9). The analyzed variables consist of 20–100-day filtered latent heat flux (LHF, indicated by green shading), OLR (indicated by a yellow bar chart), net surface solar radiation (FSNS, indicated by an orange bar chart), U850 (indicated by a purple bar chart), 30-

https://doi.org/10.5194/gmd-2023-152
Preprint. Discussion started: 30 August 2023




meter depth oceanic temperature (30-m T multiplied by 100, indicated by a black line), and SST (multiplied by 10, indicated by an orange line) which positive values are represented by an upward direction in LHF and FSNS. The graphical representation of variables marked with "(L)" employs the left y-axis, while variables marked with "(R)" utilize the right y-axis.

The decrease in LHF, which indicates a reduction in heat loss from the ocean, and the negative FSNS, indicating that solar radiation is heating the ocean, coincide with easterly zonal winds that contribute to positive SST anomaly in ERA5 (Fig. 9a). This lead–lag relationship depicts the changes in LHF, FSNS, OLR, U850 and SST which positive SST anomaly prior to the MJO convection period emphasizing the interconnectedness of oceanic heat fluxes, solar radiation, and atmospheric circulation patterns. As the MJO convection progresses through the region (110–130° E and 5–15° S), several changes in atmospheric and oceanic variables occur. These changes include a shift in OLR from positive to negative values, a decrease in SST, a transition to westerly winds, and an increase in positive FSNS and LHF (Fig. 9a). With the exception of experiments of A–CTL and C–30days, both the high-frequency and low-frequency SST feedback experiments exhibit similar simulation of lead–lag relationships when compared to ERA5 (Fig. 9c–h). It is worth noting that in experiments C–CTL, C–1day, C–3days, and C–6days, the variations in LHF are underestimated. Conversely, in experiment C–18days, the variations in LHF are overestimated. In experiment C–12days, the variations in LHF are similar to the expected values. The magnitude of SST fluctuations is directly related to the variations in LHF, FSNS, OLR, and U850 in the lead–lag relationship. In ERA5, phase 2 corresponds to the occurrence of the maximum positive SST anomaly within the domain of 110–130° E and 5–15° S, while phase 7 corresponds to the occurrence of the most negative SST anomaly. When comparing the high-frequency and low-

https://doi.org/10.5194/gmd-2023-152
Preprint. Discussion started: 30 August 2023

Geoscientific Model Development Discussions
Open Access

frequency SST feedback experiments to ERA5, except for experiments A–CTL and C–30days, the maximum positive SST anomaly is consistently delayed by one phase.

Additionally, the occurrence of the most negative SST anomaly aligns with the same phase in both types of experiments. The maximum positive anomaly in the 30-m T is delayed by one phase compared to the SST, indicating the transfer of heat from the ocean surface into the upper ocean progressively. Similarly, the occurrence of the most negative 30-m T anomaly is also delayed by one phase compared to SST, revealing the buffering role of the upper ocean when the MJO convection extracts heat (energy) from the ocean (Fig. 9c–i). In the A–CTL experiment, which utilizes monthly OISST data, the SST anomalies are relatively small. This is reflected in the weak anomalies observed in OLR and FSNS (Fig. 9b). On the other hand, in the C–30days experiment, there is a misalignment in the lead–lag relationship, and the OLR and FSNS anomalies are also weak (Fig. 9i).

### 4.3 The extreme frequency of oceanic feedback can sustain MJO propagation

In previous studies, it has been observed that most models incorporate both coupled and uncoupled simulations. DeMott et al. (2014) specifically noted that in uncoupled experiments, SPCAM3 exhibited strong eastward propagation for 5-day running means, but relatively weaker propagation for monthly means. This raises the question of how much SST feedback periodicity is necessary to maintain robust eastward propagation in coupled experiments. This section aims to discuss this topic and explore strategies for achieving robust eastward propagation. It is observed that the aforementioned criteria are met with increased feedback periodicity for SST until the C–30days experiment. SST feedback periodicity, characterized by SST-forced atmospheric variability, exhibits notable differences between coupled and uncoupled experiments. In uncoupled experiments (A–CTL), the SST lacks responsiveness to

https://doi.org/10.5194/gmd-2023-152
Preprint. Discussion started: 30 August 2023

Geoscientific Model Development Discussions

atmospheric changes, leading to unrealistic intraseasonal variability in atmospheric circulation. Spatially, Through air–sea interaction, most of the coupled experiments showed improved MJO simulation with realistic strength and eastward propagation speeds (e.g., C–CTL, C–1day, C–3days, C–6days, C–12days, and C–18days), where higher MJO variance was associated with increased SST feedback periodicity.

Generally, C–18days exhibited an overestimation of intraseasonal variability while maintaining eastward propagation of the MJO. Figure 10 highlights considerable differences in the simulation of robust (disordered) MJOs at phase 4 between C–18days and C–30days. In C–18days, negative OLR anomalies are widespread across the MC and extend to the WP near the equator in the northern hemisphere (Fig. 10b). Concurrently, U200 exhibits divergence patterns that coincide with the negative OLR anomaly. Negative OLR anomalies are indicative of the presence of deep convection. In the C–CTL experiment, the spatial distribution of negative OLR overlaps with positive net surface heat flux and solar radiation anomalies, indicating heat loss from the ocean to the atmosphere (Fig. 10g). Notably, in C–18days, there is irregular heat flux loss from the surface ocean near the equator in the western Pacific (Fig. 10h), which is not observed in C–CTL.

Furthermore, in the C–18days experiment, there is a notable 75% increase in solar radiation anomalies (with upward direction indicating positive values), resulting in reduced solar radiation reaching the ocean surface in the southeastern IO when compared to C–CTL. Positive anomalies in LHF (Fig. 10e) are predominantly observed within and the west of the convective region, coinciding with westerly winds and a cooling of SST (Fig. 10k). Liang et al. (2018) investigated the variability of the heat fluxes, a major contributor of the intraseasonal SST variability. In C–CTL at phase 4, relatively weak westerly winds and latent heat flux are observed in the IO (Fig. 10d). Upon the passage of deep convection across the MC, the IO experiences

https://doi.org/10.5194/gmd-2023-152
Preprint. Discussion started: 30 August 2023




intensified westerly winds and latent heat flux anomalies (not shown). These positive latent heat flux anomalies, resulting from ocean evaporation, contribute negative SST anomalies and provide a negative feedback in the atmosphere. Wu and Kirtman (2005) suggest that through air–sea coupling, SST-forced atmospheric changes in surface winds and heat fluxes exert a strong negative feedback on SSTs in the Indo-Pacific region. Jayakumar et al. (2011) conducted a series of experiments using an ocean general circulation model to investigate the individual contributions of different processes. Their findings during the period of 1997–2006 reveal that wind stress accounted for approximately 20% of the intraseasonal SST variability in the IO region, while heat fluxes made up about 70% of the variability. Among the heat flux components, shortwave radiation exerted the most significant influence, contributing 75%, while the remaining 25% was attributed to other flux components. Gao et al. (2020a) corroborate that the temporal variations in SST anomaly are primarily driven by shortwave radiative heating, and LHF playing a secondary role.

In both C–CTL and C–18days simulations, there is evidence of a negative feedback in the lag–lead relationships among SST, surface winds, rainfall anomalies, and heat fluxes (Fig. 9c and 9h), which supports the findings of previous studies (Wu and Kirtman, 2005; Jayakumar et al., 2011; Gao et al., 2020a). With increased feedback periodicity of SST in C–CTL and C–18days, the ocean continues to receive atmospheric forcing, but the feedback response is delayed, leading to the accumulation of energy (temperature) in the upper ocean, as seen in the SST distribution in the WP (Fig. 10k). In C–30days, SST exhibits a perturbed unrealistically spatial distribution (Fig. 10l) driven by plus-minus latent heat flux and 10m wind anomalies (Fig. 10f), net surface heat flux, and solar radiation (Fig. 10i). Consequently, these perturbed SST plus-minus patterns trigger numerous local

https://doi.org/10.5194/gmd-2023-152
Preprint. Discussion started: 30 August 2023

Geoscientific Model Development Discussions

convections among the IO, MC, and WP and does not manifest as organized the large-scale circulation.

### 4.4 The moist static energy (MSE) analysis

A budget analysis of MSE is used to investigate the underlying mechanisms driving the onset and eastward propagation of the MJO event. Analyzing the MSE budget provides valuable insights into the physical processes and feedback mechanisms influencing the behavior of the MJO, including vertical MSE advection, zonal MSE advection, meridional MSE advection, surface heat fluxes, atmospheric radiative term, and residual components.

#### 4.4.1 Preconditioning phase

Analysis of the column-integrated MSE budget has revealed that both vertical and horizontal MSE advection contribute to the east-west asymmetry of MSE tendency, thereby facilitating the eastward propagation of the MJO (Wang and Li, 2020). Figure 11 illustrates the physical processes associated with each term contributing to the column-integrated MSE tendency (<dmdt>) in Eq. (1), as outlined in Tseng et al. (2022), preceding deep convection over the MC area (10° S–0° N/S, 120–150° E) during phase 2 over the ERA5 and model simulations. The MJO convection in the eastern Indian Ocean at phase 2, the column-integrated vertical advection (-<wdmdp>) over the MC area takes a dominant role in the MSE budget, while horizontal MSE advection (-<vdm>) plays a secondary role. These findings, along with significant compensation from longwave radiation, were identified by Wang and Li (2020) and Tseng et al. (2022). Generally, the -<wdmdp> accounts for approximately 72–86% of ERA5, except for A–CTL and C–30days, while the -<vdm> increases from 40% to 80% of ERA5 due to the heightened feedback

https://doi.org/10.5194/gmd-2023-152
Preprint. Discussion started: 30 August 2023




periodicity of SST (Fig. 11). Those results indicate that all model simulations exhibit weaker 20–100-day filtered MSE advection anomalies prior to the eastward propagation of the MJO over the MC compared to ERA5. Similarly, the precipitation results in Fig. 4c–h demonstrate the same trend. Moreover, the LH term exhibits an opposite trend to the -<vdm> term due to the increased feedback periodicity of SST, while SH and shortwave radiation fluxes (<SW>) contribute less to the negative MSE tendency in both ERA5 and model simulations. These findings indicate that, in the early phase, the negative contribution primarily stems from the LH and longwave radiation fluxes (<LW>) term. Tseng et al. (2022) identify the negative LH bias as a key factor in enhancing the leading MSE tendency during MJO preconditioning phases. In general, coupling enhances the budget simulation by increasing the positive contribution of vertical and horizontal advection and the negative contribution of LH and <LW> in MSE tendency, primarily due to the intensified feedback periodicity of SST during the initial phase of the MJO. Although the <dmdt> term can be further decomposed into variations of <wdmdp>, <vdm>, and LH in model simulations, the total column-integrated MSE tendency does not exhibit a clear difference in response to the increasing feedback periodicity of SST experiments during the initial phase of the MJO.

#### 4.4.2 Phase of strongest convection across the MC

We compared the spatial distribution of 20–100-day <dmdt> (shading), precipitation (contours), and 850-hPa wind (vectors) during phase 5, which represents the period of strongest convection across the MC (Fig. 12). In ERA5, the main convection is accompanied by positive precipitation anomalies and low-level convergence in the 850-hPa wind across the MC extending into the WP (Fig. 12a). A positive MSE tendency, peaking near 15° N and 15° S, is observed to the east of the

https://doi.org/10.5194/gmd-2023-152
Preprint. Discussion started: 30 August 2023

Geoscientific Model Development
Discussions
Open Access

MJO convection located near the Equator. Conversely, a negative integrated MSE tendency is observed to the west of the MJO convection accompanied by negative precipitation anomalies to the west of this region. The meridionally confined structure near the Equator exhibits characteristics indicative of an equatorial Kelvin wave propagated toward the east as fundamental dynamics of the MJO. With the exception of A–CTL and C–30days, the model simulations display a similar structure to ERA5 in terms of the 20–100-day filtered <dmdt>, precipitation, and 850-hPa wind vectors (Fig. 12c–h). C–CTL exhibits relatively weak precipitation anomalies in the MC and weak westerly winds in the IO until C–6days, where robust precipitation and low-level convergence in the 850-hPa wind occur in response to the feedback periodicity of SST increasing. On the contrary, A–CTL exhibits abnormal positive precipitation anomalies distributed over the western IO, while localized maximum of <dmdt> occur near 15° N (Fig. 12b). In contrast, C–30days displays plus-minus precipitation anomalies near the Equator, consequently disrupting the spatial distribution of the <dmdt> relative to MJO convection (Fig. 12i).

To quantify the impact of SST feedback periodicity on atmospheric intraseasonal variability in the tropics, we adopt the approach of Tseng et al. (2022) and Jiang et al. (2018) to project all MSE terms onto the 20–100-day filtered ERA5 <dmdt> (Fig. 12a) during phase 5. The MC has been frequently identified as a barrier to the eastward propagation of the MJO, as noted by Li et al. (2020b). Additionally, a considerable proportion, approximately 30–50%, of the MJO experiences stalling over the MC, as reported by Zhang and Han (2020). To mitigate the influence of weaker MJO events that dissipate prior to reaching the MC, our focus is specifically on phase 5 of the MJO. Figure 13(a) illustrates the determination of the contribution of each component of the MSE tendency during phase 5 by projecting the spatial pattern of each MSE budget term over the MC region (20° S–20° N, 90–210° E),

https://doi.org/10.5194/gmd-2023-152
Preprint. Discussion started: 30 August 2023

Geoscientific Model Development Discussions

where $F_s$ is total surface fluxes including sensible and latent heat fluxes, and $Q_r$ is vertically integrated radiative (short-wave and long-wave) heat fluxes. The dominant contribution of horizontal advection to the MSE tendency (Fig. 13a) are simulated well in both the high-frequency and low-frequency SST feedback experiments, but not in the A–CTL simulation. The -<vdm> term increases in response to the increasing feedback periodicity of SST, resulting from stronger low-level convergence, which enhances MJO convection. Vertical advection -<wdmdp> is not the dominant term over the MC region (20° S–20° N, 90–210° E) in both ERA5 and model simulations during phase 5. Furthermore, Fs and Qr make a minor contribution to the MSE tendency, with the sensible and latent heat fluxes exhibiting a tendency towards greater recessive behavior in response to the increasing feedback periodicity of SST.

The total horizontal MSE advection is further decomposed into its zonal (-<udmdx>) and meridional zonal (-<vdmdy>) components for high-frequency SST feedback experiments (C–CTL, A–CTL, C–1day, and C–3days) and low-frequency SST feedback experiments (C–6days, C–12days, C–18days, and C–30days) in order to examine their individual effects (Fig. 13b–c). Both components contribute positively, but the -<vdmdy> exhibits a larger amplitude, consistent with findings by Tseng et al. (2022) during phase 4. The -<vdmdy> of high-frequency SST feedback experiments (C–CTL, C–1day, and C–3days) closely resemble ERA5 in terms of the projected magnitude. Comparatively, the -<vdmdy> term in low-frequency SST feedback experiments (C–6days, C–12days, C–18days, and C–30days) exhibits a more positive contribution than in high-frequency SST experiments, leading to a dominant contribution to the increase in -<vdm> and <dmdt>.

We generated a spatial representation of the 20–100-day column-integrated vertical MSE advection (J $kg^{-1}$ $s^{-1}$, represented by shading), column-integrated

https://doi.org/10.5194/gmd-2023-152
Preprint. Discussion started: 30 August 2023

Geoscientific Model Development
Discussions

horizontal MSE advection (J $kg^{-1}$ $s^{-1}$, shown as contours with an interval of 6.0), and 200-hPa wind (green vectors) relative to a reference vector (3 m $s^{-1}$) during phase 5 (Fig. 14). This figure complements the information provided by the bar chart in Fig. 13a. In ERA5, the wind divergence at 200 hPa during phase 5 (Fig. 14a), overlaid with the 850-hPa convergence (Fig. 12a), indicates a vertically tilting structure of zonal wind anomalies. Except for A–CTL and C–30days, the model simulations exhibit a similar structure to ERA5 in terms of low-level convergence and high-level divergence. In ERA5, the negative -<wdmdp> and -<vdm> anomalies (Fig. 14a) are observed to the west of the MJO convection, which is characterized by positive precipitation anomalies (Fig. 12a). The spatial distribution of the negative -<vdm> anomaly (dashed-red contours) extends from the IO to the MC, exhibiting a pattern similar to <dmdt> with enhanced anomalies. This results in the projection of the spatial pattern of the -<vdm> term being greater than 1. The positive -<wdmdp> anomaly (shading) is located in the western IO and east of the dateline, which results in a spatial distribution unlike that of <dmdt> comparatively. This difference reduces the projection of the spatial pattern of -<vdm> to a value lower than 1. On the contrary, in the A–CTL experiment, the positive -<vdm> anomaly (solid-blue contours) exhibits a spatial distribution near 120° E (Fig. 14b), while the negative -<vdm> anomaly (dashed-red contours) is distributed on both the positive left and right sides. Although the negative -<vdm> anomaly in high-frequency SST feedback experiments (C–CTL, C–1day, and C–3days) underestimates that of ERA5 (Fig. 14c–e), the spatial distribution remains similar to ERA5 due to an approximately 80% projection of -<vdm> compared to ERA5. The low-frequency SST feedback experiments (C–6days, C–12days, and C–18days) yield greater -<vdm> anomalies (Fig. 14f–h) compared to ERA5, with projection values greater than 1. We noticed that, in the low-frequency SST feedback experiments, although the anomalies of -

https://doi.org/10.5194/gmd-2023-152
Preprint. Discussion started: 30 August 2023

Geoscientific Model Development Discussions
Open Access

<wdmdp> intensify, the spatial distribution of those shift eastward, leading to a decrease in projection values.

## 5. Conclusions

This study builds upon the work of Lan et al. (2022) and Tseng et al. (2022) by coupling a high-resolution 1-D TKE ocean model (the SIT model) with the CAM5, specifically the CAM5–SIT configuration, to investigate the extreme effects of interseasonal SST feedback on the MJO. We introduced asymmetric exchange frequencies between the atmosphere and the ocean, ensuring bidirectional interaction at each timestep within the experimental periodicity by fixing the SST value in the Coupler. This allowed us to create various intraseasonal SST feedback atmospheric experiments, including intervals of 30 minutes, 1, 3, 6, 12, 18, and 30 days. Systematic sensitivity experiments were conducted to divide into two groups: those feedback periodicity within a phase (high-frequency SST) and those beyond a phase (low-frequency SST).

The aim is to assess the scientific reproducibility and consistency of the findings across different SST feedback cycles in the field of modeling science. With the exception of the C–30days experiment, both the high-frequency (C–CTL, C–1day, and C–3days) and low-frequency (C–6days, C–12days, C–18days) experiments demonstrate realistic simulations of various aspects of the MJO when compared to ERA5. These aspects include intraseasonal periodicity (as shown in Fig. 1), eastward propagation (as observed in Fig. 2 and 4), coherence in the low-frequency band (as depicted in Fig. 3), tilting vertical structure (evident in Fig. 5, 12, and 14 for zonal wind), intraseasonal SST (as summarized in Table 2) and oceanic temperature variances (as shown in Fig. 7), the lead–lag relationship of intraseasonal variability (as characterized in Fig. 9), phase 2 column-integrated MSE tendency terms

https://doi.org/10.5194/gmd-2023-152
Preprint. Discussion started: 30 August 2023

Geoscientific Model Development
Discussions

(including decomposition items) (illustrated in Fig. 11), and the projection of all MSE terms onto the ERA5 column-integrated MSE tendency during phase 5 (depicted in Fig. 13).

The lead–lag relationship provides a visual representation of the variations in 20–100-day filtered LHF, FSNS, OLR, U850 and SST, while positive SST leading up to the onset of the MJO convection (Fig. 9). This relationship highlights the interconnected nature of oceanic heat fluxes, solar radiation, and atmospheric circulation patterns, underscoring their mutual influence and interplay. Table 3 provides a comprehensive overview of several variables during the boreal winter, including the average values of 20–100-day filtered OLR, LHF, FSNS, U850, <dmdt>, -<wdmdp>, and -<vdm>. These variables are categorized based on the states of SST warming and cooling. The categorization is performed over two specific domains: (110–130° E, 5–15° S), as referenced in Fig. 9, and (120–150° E, 0–10° S) marked as background gray, as referenced in Fig. 11. We highlight the characteristics of the MJO-related atmosphere with red letters, which correspond closely to the values in ERA5. In synthesizing the findings from Arnold et al. (2013) regarding the high SST enhances MJO simulation, the improved MJO simulation through intraseasonal SST variability by Liang et al. (2018), the information provided in Tables 2 and 3, and the corresponding figures, it becomes evident that the high-frequency (low-frequency) SST experiments tended to underestimate (overestimate) the MJO simulation. Notably, the experiment C–6days demonstrated the closest similarity to ERA5 in terms of MJO simulation.

Among the high-frequency experiments, C–3days shows a less close resemblance to the observed MJO characteristics. The result of the C–3days experiment is consistent with Stan (2018), as the absence of 1–5-day variability in SST promotes the amplification of westward power associated with Rossby waves. In addition, the C–1day experiment confirms the scientific reproducibility of Hagos et al. (2016) and Lan et al. (2022) that demonstrates that the removal of the diurnal cycle enhances the MJO.

The increasing feedback periodicity of SST in low-frequency experiments leads to the accumulation of short-wave and long-wave radiations and surface heat fluxes from the atmosphere, resulting in an increase in the upper oceanic temperature and its variances (Table 2). SST variances that are higher than OISST contribute to robust/overestimated simulations of the MJO (as observed in Fig. 1–14 and Table 3). In contrast, the C–30days experiment exhibits variances with both positive and negative anomalies in precipitation (Fig. 4 and 10), oceanic temperature (Fig. 7), net surface heat fluxes (Fig. 10), and column-integrated vertical and horizontal MSE advection (Fig. 14). These anomalies have an unrealistically spatial distribution and an unrealistic vertical tilting structure in both specific humidity and air temperature anomalies (Fig. 5i) over the Indo-Pacific region. As a result, local convection appears randomly among the IO, MC, and WP, and does not manifest as organized MJO convection.

Finally, in Fig. 15, the interseasonal SST feedback experiments on MJO are depicted schematically. These experiments include the uncoupled model (A–CTL), high-frequency SST experiments (C–CTL, C–1day, and C–3days), low-frequency SST experiments (C–6days, C–12days, C–18days), and disorganized convection and circulation (C–30days) which figure concept is based on DeMott et al. (2014) in Fig. 11. In the absence of interseasonal SST variability, the uncoupled A–CTL disrupts the eastward propagation of the MJO, leading to weakened or fragmented MJO activity as shown in Fig. 15a. On the other hand, the high-frequency SST experiments generally capture the characteristics of the MJO. The time-varying SSTs in the coupled simulation provide a certain level of organization and sufficient surface fluxes, which

https://doi.org/10.5194/gmd-2023-152
Preprint. Discussion started: 30 August 2023




facilitate the development of MJO circulations, as illustrated in Fig. 15b. Moreover, in the coupled model, the presence of land convection over the MC ahead of the MJO convection (Fig. 6) contributes to the instability and uplift of moist air masses. Conventionally, the MJO has been regarded as a tropical atmospheric variability, given that its existence is primarily attributed to the interplay between organized convection and large-scale circulations. This dynamic process plays a crucial role in triggering the eastward propagation of the MJO. Furthermore, the low-frequency SST experiments demonstrate robust simulations of the MJO. This can be attributed comprehensively to the increased SST variances, accumulation of surface fluxes, enhanced low-level convergence (Fig. 12) and high-level divergence (Fig. 14), as well as horizontal MSE advection, as depicted in Fig. 15c. On the other hand, the C–30days experiment simulates frequent, disorganized convection, as shown in Fig. 15d. This experiment exhibits both positive and negative anomalies in precipitation, SST, surface heat fluxes, and vertical and horizontal MSE advection, which fail to generate the expected circulation anomalies.

*Code and data availability.* The model code of CAM5–SIT is available at https://doi.org/10.5281/zenodo.5510795. Input data of CAM5–SIT using the climatological Hadley Centre Sea Ice and Sea Surface Temperature dataset and GODAS data forcing, including 30-year numerical experiments, are available at https://doi.org/10.5281/zenodo.5510795.

*Author contributions.* HHH is the initiator and the primary investigator of the Taiwan Earth System Model project. YYL is the CAM5–SIT model developer and writes the majority part of the paper. WLT assists in MSE analysis.

https://doi.org/10.5194/gmd-2023-152
Preprint. Discussion started: 30 August 2023

Geoscientific Model Development Discussions
Open Access

*Competing interests*. The authors declare that they have no conflict of interest.

*Acknowledgements*. The contribution from YYL, HHH, and WLT to this study is supported by Ministry of Science and Technology of Taiwan under contracts MOST 110-2123-M-001-003, MOST 110-2811-M-001-603, MOST 109-2811-M-001-624 and MOST108-2811-M-001-643. Our deepest gratitude goes to the editors and anonymous reviewers for their careful work and thoughtful suggestions that have helped improve this paper substantially. We sincerely thank the National Center for Atmospheric Research and their Atmosphere Model Working Group (AMWG) for release CESM1.2.2. We thank the computational support from National Center for High530 performance Computing of Taiwan. Thanks, ChatGPT for correcting the English grammar.

https://doi.org/10.5194/gmd-2023-152
Preprint. Discussion started: 30 August 2023




**Reference**

Adler, R. F., Huffman, G. J., Chang, A., Ferraro, R., Xie, P. P., Janowiak, J., Rudolf, B., Schneider, U., Curtis, S., Bolvin, D., Gruber, A., Susskind, J., Arkin, P., and Nelkini, E.: The Version 2.1 Global Precipitation Climatology Project (GPCP) Monthly Precipitation Analysis (1979 -Present), J. Hydrometeor., 4(6), 1147-1167, https://doi.org/10.1175/1525-7541(2003)004<1147:TVGPCP>2.0.CO;2, 2003.

Amante, C., and Eakins, B. W.: ETOPO1 1 arc-minute globe relief model: Procedures, data sources and analysis, NOAA Tech. Memo. NESDIS NGDC-24, NOAA, Silver Spring, MD, 19 pp., https://doi.org/10.7289/V5C8276M, 2009.

Arnold, N. P., Kuang, Z., and Tziperman, E.: Enhanced MJOlike variability at high SST, J. Climate, 26, 988–1001, https://doi.org/10.1175/JCLI-D-12-00272.1, 2013.

Banzon, V. F., Reynolds, R. W., Stokes, D., and Xue, Y.: A 1/4-spatial-resolution daily sea surface temperature climatology based on a blended satellite and in situ analysis, J. Climate, 27, 8221–8228, https://doi.org/10.1175/JCLI-D-14-00293.1, 2014.

Behringer, D. W., and Xue, Y.: Evaluation of the global ocean data assimilation system at NCEP: The Pacific Ocean. Eighth Symposium on Integrated Observing and Assimilation Systems for Atmosphere, Oceans, and Land Surface, AMS 84th Annual Meeting, Washington State Convention and Trade Center, Seattle, Washington, 11-15. Derber, J.C., and A. Rosati, 1989: A global oceanic data assimilation system, J. Phys. Oceanogr., 19, 1333–1347, https://ams.confex.com/ams/pdfpapers/70720.pdf, 2004.

Chang, M.-Y., Li, T., Lin, P.-L., and Chang, T.-H.: Forecasts of MJO Events during DYNAMO with a Coupled Atmosphere-Ocean Model: Sensitivity to Cumulus Parameterization Scheme, J. Meteorol. Res., 33, 1016–1030, https://doi.org/10.1007/s13351-019-9062-5, 2019.

CLIVAR MADDEN–JULIAN OSCILLATION WORKING GROUP: MJO simulation diagnostics, J. Climate, 22, 3006–3030, https://doi.org/10.1175/2008JCLI2731.1, 2009.

DeMott, C. A., Klingaman, N. P., and Woolnough, S. J.: Atmosphere-ocean coupled processes in the Madden-Julian oscillation, Rev. of Geophysics, 53, 1099– 1154, https://doi.org/10.1002/2014RG000478, 2015.

DeMott, C. A., Stan, C., Randall, D. A., and Branson, M. D.: Intraseasonal variability in coupled GCMs: The roles of ocean feedbacks and model physics, J. Climate, 27(13), 4970– 4995. https://doi.org/10.1175/JCLI-D-13-00760.1., 2014.

https://doi.org/10.5194/gmd-2023-152
Preprint. Discussion started: 30 August 2023





de Boisséson, E., Balmaseda, M. A., Vitart, F., and Mogensen, K.: Impact of the sea surface temperature forcing on hindcasts of Madden-Julian Oscillation events using the ECMWF model, Ocean Sci., 8, 1071–1084, https://doi.org/10.5194/os-8-1071-2012, 2012.

de Szoeke, S. P., Edson, J. B., Marion, J. R., Fairall, C. W., and Bariteau, L.: The MJO and air–sea interaction in TOGA COARE and DYNAMO, J. Climate, 28(2), 597– 622. https://doi.org/10.1175/JCLI-D-14-00477.1, 2014.

de Szoeke, S. P., and Maloney, E.: Atmospheric mixed layer convergence from observed MJO sea surface temperature anomalies, J. Climate, 33(2), 547– 558. https://doi.org/10.1175/JCLI-D-19-0351.1, 2020.

Fu, J. X., Wang, W., Shinoda, T., Ren, H. L., and Jia, X.: Toward understanding the diverse impacts of air–sea interactions on MJO simulations, J. Geophys. Res.-Oceans,122(11), 8855– 8875. https://doi.org/10.1002/2017JC013187, 2017.

Fuchs, Ž., and Raymond, D. J.: A simple model of intraseasonal oscillations, J. Adv. Model. Earth Syst., 9, 1195–1211. https://doi.org/10.1002/2017MS000963, 2017.

Hagos, S. M., Zhang, C., Feng, Z., Burleyson, C. D., Mott, C. De, Kerns, B., Benedict, J. J., and Martini, M. N.: The impact of the diurnal cycle on the propagation of Madden-Julian Oscillation convection across the Maritime Continent, J. Adv. Model. Earth Syst., 8, 1552–1564, https://doi.org/10.1002/2016MS000725, 2016.

Hersbach, H., and Dee, D.: ERA5 reanalysis is in production, ECMWF Newsletter, Vol. 147, p. 7, https://www.ecmwf.int/en/newsletter/147/news/era5-reanalysis-production, 2016.

Gao, Y., Hsu, P.-C., Chen, L., Wang, L., and Li, T.: Effects of high-frequency surface wind on the intraseasonal SST associated with the Madden-Julian oscillation, Clim. Dynam., 54, 4485–4498, https://doi.org/10.1007/s00382-020-05239-w, 2020a.

Gao, Y., Klingaman, N. P., DeMott, C. A., and Hsu, P.-C.: Boreal summer intraseasonal oscillation in a superparameterized general circulation model: effects of air–sea coupling and ocean mean state, Geosci. Model Dev., 13, 5191–5209, https://doi.org/10.5194/gmd-13-5191-2020, 2020b.

Ge, X., Wang, W., Kumar, A., and Zhang, Y.: Importance of the vertical resolution in simulating SST diurnal and intraseasonal variability in an oceanic general circulation model, J. Climate, 30, 3963–3978, https://doi.org/10.1175/JCLI-D-16-0689.1, 2017.

https://doi.org/10.5194/gmd-2023-152
Preprint. Discussion started: 30 August 2023

Geoscientific Model Development
Discussions

Hong, X., Reynolds, C. A., Doyle, J. D., May, P., and O'Neill, L.: Assessment of upper-ocean variability and the Madden-Julian Oscillation in extended-range air–ocean coupled mesoscale simulations, Dyn. Atmos. Oceans, 78, 89–105. https://doi.org/10.1016/j.dynatmoce.2017.03.002, 2017.

Hsu, J.-Y., Hendon, H., Feng, M., and Zhou, X.: Magnitude and phase of diurnal SST variations in the access-S1 model during the suppressed phase of the MJOs, J. Geophys. Res.-Oceans, 124 (2019), pp. 9553-9571, https://doi.org/10.1029/2019JC015458, 2019.

Hsu, P.-C., and Li, T.: Role of the boundary layer moisture asymmetry in causing the eastward propagation of the Madden–Julian oscillation, J. Climate, 25:4914–4931, https://doi.org/10.1175/JCLI-D-11-00310.1, 2012.

Jayakumar, A., Vialard, J., Lengaigne, M., Gnanaseelan, C., McCreary, J.P., and Kumar, B.P.: Processes controlling the surface temperature signature of the Madden-Julian oscillation in the thermocline ridge of the Indian Ocean, Clim. Dynam., 37, 2217–2234, https://doi.org/10.1007/s00382-010-0953-5, 2011.

Jiang, X.,Waliser, D. E., Xavier, P. K., Petch, J., Klingaman, N. P., Woolnough, S. J., Guan, B., Bellon, G., Crueger, T., DeMott, C., Hannay, C., Lin, H., Hu, W., Kim, D., Lappen, C.-L., Lu, M.-M., Ma, H.-Y., Miyakawa, T., Ridout, J. A., Schu-bert, S. D., Scinocca, J., Seo, K.-H., Shindo, E., Song, X., Stan, C., Tseng, W.-L., Wang, W., Wu, T., Wu, X., Wyser, K., Zhang, G. J., and Zhu, H.: Vertical structure and physical processes of the MaddenJulian oscillation: Exploring key model physics in climate simulations, J. Geophys. Res.-Atmos., 120, 4718–4748, https://doi.org/10.1002/2014JD022375, 2015.

Jiang, X., Adames, Á. F., Zhao, M., Waliser, D., and Maloney, E.: A unified moisture mode framework for seasonality of the Madden–Julian oscillation, J. Climate, 31, 4215–4224, https://doi.org/10.1175/JCLI-D-17-0671.1, 2018.

Jiang, X., Adames, Á. F., Kim, D., Maloney, E. D., Lin, H., and Kim, H., Zhang, C., DeMott, C. A., and Klingaman, N. P.: Fifty years of research on the Madden-Julian Oscillation: Recent progress, challenges, and perspectives, J. Geophys. Res.-Atmos., 125, e2019JD030911, https://doi.org/10.1029/2019JD030911, 2020.

Kang, D., Kim, D., Ahn, M. S., Neale, R., Lee, J., and Gleckler, P. J.: The role of the mean state on MJO simulation in CESM2 ensemble simulation, Geophys. Res. Lett., 47, e2020GL089824. https://doi.org/10.1029/2020GL089824, 2020.

Kim, H., Vitart, F., and Waliser, D. E.: Prediction of the Madden–Julian oscillation: A review, J. Climate, 31(23), 9425– 9443, https://doi.org/10.1175/JCLI-D-18-0210.1, 2018.

https://doi.org/10.5194/gmd-2023-152
Preprint. Discussion started: 30 August 2023

Geoscientific Model Development Discussions

Klingaman, N. P., and Demott, C. A,: Mean state biases and interannual variability affect perceived sensitivities of the Madden-Julian oscillation to air–sea coupling, J. Adv. Model. Earth Syst., 12, 1– 22, https://doi.org/10.1029/2019MS001799, 2020.

Krishnamurti, T. N., Oosterhof, D. K. and Mehta, A. V.: Air–sea interaction on the time scale of 30 to 50 days, J. Atmos. Sci., 45, 1304–1322, https://doi.org/10.1175/1520-0469(1988)045,1304:AIOTTS.2.0.CO;2, 1988.

Lambaerts, J., Lapeyre, G., Plougonven, R., and Klein, P.: Atmospheric response to sea surface temperature mesoscale structures, J. Geophys. Res.-Atmos., 118(17), 9611–9621. https://doi.org/10.1002/jgrd.50769, 2020.

Lan, Y.-Y., Tsuang, B.-J., Tu, C.-Y., Wu, T.-Y., Chen, Y.-L., and Hsieh, C.-I.: Observation and Simulation of Meteorology and Surface Energy Components over the South China Sea in Summers of 2004 and 2006, Terr. Atmos. Ocean. Sci., 21, 325–342, https://doi.org/ 10.3319/TAO.2009.04.07.01(A), 2010.

Lan, Y.-Y., Hsu, H.-H., Tseng, W.-L., and Jiang, L.-C.: Embedding a one-column ocean model in the Community Atmosphere Model 5.3 to improve Madden–Julian Oscillation simulation in boreal winter, Geosci. Model Dev., 15, 5689–5712, https://doi.org/10.5194/gmd-15-5689-2022, 2022.

Li, Y., Han, W., Shinoda, T., Wang, C., Ravichandran, M., and Wang, J.-W.: Revisiting the wintertime intraseasonal SST variability in the tropical south Indian Ocean: Impact of the ocean interannual variation, J. Phys. Oceanogr., 44, 1886–1907, https://doi.org/10.1175/JPO-D-13-0238.1, 2014.

Li, T., Ling, J., and Hsu, P.-C.: Madden–Julian Oscillation: Its discovery, dynamics, and impact on East Asia, J. Meteor. Res., 34, 20–42, https://doi.org/10.1007/s13351-020-9153-3, 2020a.

Li, K., Yu, W., Yang, Y., Feng, L., Liu, S., and Li, L.: Spring barrier to the MJO eastward propagation, Geophys. Res. Lett., 47, e2020GL087788, https://doi.org/10.1029/2020GL087788, 2020b.

Liang, Y.; Du, Y.; Zhang, L.; Zheng, X.; Qiu, S. The 30−50-Day Intraseasonal Oscillation of SST and Precipitation in the South Tropical Indian Ocean, Atmos., 9, 69. https://doi.org/10.3390/atmos9020069, 2018.

Liang, Y., and Du, Y.: Oceanic impacts on 50–80-day intraseasonal oscillation in the eastern tropical Indian Ocean, Clim. Dynam., 59, 1283–1296, https://doi.org/10.1007/s00382-021-06041-y, 2022.

Liebmann, B.: Description of a complete (interpolated) outgoing longwave radiation dataset, B. Am. Meteorol. Soc., 77, 1275–1277,

https://doi.org/10.5194/gmd-2023-152
Preprint. Discussion started: 30 August 2023




1996.

Madden, R. A., and Julian, P. R.: Description of global-scale circulation cells in the tropics with a 40-50 day period, J. Atmos. Sci., 29, 1109-1123, https://doi.org/10.1175/1520-0469(1972)029<1109:DOGSCC>2.0.CO;2, 1972.

Newman, M., Sardeshmukh, P. D., and Penland, C.: How important is air–sea coupling in ENSO and MJO evolution? J. Climate, 22, 2958– 2977, https://doi.org/10.1175/2008JCLI2659.1, 2009.

Pariyar, S.K., Keenlyside, N., Tseng, W.-L., Hsu, H.-H., and Tsuang, B.-J. The role of air–sea coupling on November–April intraseasonal rainfall variability over the South Pacific, Clim. Dynam., 60, 1121–1136, https://doi.org/10.1007/s00382-022-06354-6, 2023.

Pei, S., Shinoda, T., Soloviev, A., and Lien, R.-C.: Upper ocean response to the atmospheric cold pools associated with the Madden-Julian Oscillation, Geophys. Res. Lett., 45, 5020–5029, https://doi.org/10.1029/2018GL077825, 2018.

Rayner, N. A., Parker, D. E., Horton, E. B., Folland, C. K., Alexander, L. V., Rowell, D. P., Kent, E. C., and Kaplan, A.: Global analyses of sea surface temperature, sea ice, and night marine air temperature since the late nineteenth century, J. Geophys. Res., 108(D14), 4407, https://doi.org/10.1029/2002JD002670, 2003.

Ren, P. F., Gao, L., Ren, H.-L., Rong, X., and Li, J.: Representation of the Madden–Julian Oscillation in CAMSCSM, J. Meteor. Res., 33, 627–650, https://doi.org/10.1007/s13351-019-8118-x, 2019.

Savarin, A., and Chen, S. S.: Pathways to better prediction of the MJO: 2. Impacts of atmosphere-ocean coupling on the upper ocean and MJO propagation, J. Adv. Model. Earth Syst., 14, e2021MS002929, https://doi.org/10.1029/2021MS002929, 2022.

Sentić, S., Fuchs-Stone, Ž., and Raymond, D. J.: TheMadden-Julian Oscillation and meaneasterly winds, J. Geophys. Res.-Atmos., 125,e2019JD030869. https://doi.org/10.1029/2019JD030869, 2020.

Sobel, A., Wang, S., and Kim, D.: Moist static energy budget of the MJO during DYNAMO, J. Atmos. Sci., 71(11), 4276– 4291, https://doi.org/10.1175/JAS-D-14-0052.1, 2014.

Seo, H., Subramanian, A. C., Miller, A. J., and Cavanaugh, N. R.: Coupled impacts of the diurnal cycle of sea surface temperature on the Madden–Julian oscillation, J. Climate, 27(22), 8422– 8443. https://doi.org/10.1175/JCLI-D-14-00141.1, 2014.

Shinoda, T., Pei, S., Wang, W., Fu, J. X., Lien, R.-C., Seo, H., and Soloviev, A.: Climate process team: Improvement of ocean

https://doi.org/10.5194/gmd-2023-152
Preprint. Discussion started: 30 August 2023



component of NOAA climate forecast system relevant to Madden-Julian Oscillation simulations, J. Adv. Model. Earth Syst., 13(12), e2021MS002658. https://doi.org/10.1029/2021MS002658, 2021.

Stan, C.: The role of SST variability in the simulation of the MJO, Clim. Dynam., 51, 2943–2964, https://doi.org/10.1007/s00382-017-4058-2, 2018.

Tseng, W.-L., Tsuang, B.-J., Keenlyside, N. S., Hsu, H.-H. and Tu, C.-Y.: Resolving the upper-ocean warm layer improves the simulation of the Madden-Julian oscillation, Clim. Dynam., 44, 1487–1503, https://doi.org/10.1007/s00382-014-2315-1, 2015.

Tseng, W.-L., Hsu, H.-H., Lan, Y.-Y., Lee, W.-L., Tu, C.-Y., Kuo, P.-H., Tsuang, B.-J., and Liang, H.-C.: Improving Madden–Julian oscillation simulation in atmospheric general circulation models by coupling with a one-dimensional snow–ice–thermocline ocean model, Geosci. Model Dev., 15, 5529–5546, https://doi.org/10.5194/gmd-15-5529-2022, 2022.

Voldoire, A., Roehrig, R., Giordani, H., Waldman, R., Zhang, Y., Xie, S., and Bouin, M.-N.: Assessment of the sea surface temperature diurnal cycle in CNRM-CM6-1 based on its 1D coupled configuration, Geosci. Model Dev., 15, 3347–3370, https://doi.org/10.5194/gmd-15-3347-2022, 2022.

Wang, W., Hung, M.-P., Weaver, S. J., Kumar, A., and Fu, X.: MJO prediction in the NCEP Climate Forecast System version 2, Clim. Dynam., 42, 2509–2520, https://doi.org/10.1007/s00382-013-1806-9, 2014.

Wang, B., Liu, F., and Chen, G.: A trio-interaction theory for Madden–Julian oscillation, Geosci. Lett., 3(1), 1-16. https://doi.org/10.1186/s40562-016-0066-z, 2016.

Wang, L. and Li, T.: Effect of vertical moist static energy advection on MJO eastward propagation: Sensitivity to analysis domain, Clim. Dynam., 54, 2029–2039, https://doi.org/10.1007/s00382-019-05101-8, 2020.

Wheeler, M. C., and Hendon, H. H.: An all-season real-time multivariate MJO index: development of an index for monitoring and prediction, Mon. Weather Rev., 132, 1917–1932, https://doi.org/10.1175/1520-0493(2004)132<1917:AARMMI>2.0.CO;2, 2004.

Wheeler, M., and Kiladis, G. N.: Convectively coupled equatorial waves: Analysis of clouds and temperature in the wavenumber-frequency domain, J. Atmos. Sci., 56, 374– 399, https://doi.org/10.1175/1520-0469(1999)056<0374:CCEWAO>2.0.CO;2, 1999.

Wu, R. G., and Kirtman, B. P.: Roles of Indian and Pacific Ocean air–sea coupling in tropical atmospheric variability, Clim. Dynam., 25,

https://doi.org/10.5194/gmd-2023-152
Preprint. Discussion started: 30 August 2023


Geoscientific Model Development Discussions

155–170, https://doi.org/10.1007/s00382-005-0003-x, 2005.

Zhang, L., and Han, W.: Barrier for the eastward propagation of Madden–Julian Oscillation over the maritime continent: A possible new mechanism, Geophys. Res. Lett., 47(21), e2020GL090211. https://doi.org/10.1029/2020gl090211, 2020.

Zhao, N., and Nasuno, T.: How Does the Air–Sea Coupling Frequency Affect Convection During the MJO Passage?, J. Adv. Model. Earth Sy., 12, e2020MS002058, https://doi.org/10.1029/2020MS002058, 2020.

https://doi.org/10.5194/gmd-2023-152
Preprint. Discussion started: 30 August 2023



Table 1. Two sets of marine feedback frequency with high-frequency SST feedback (C–CTL, C–1day and C–3days) and low-frequency SST feedback (C–6days, C–12days, C–18days and C–30days) under SST sub-seasonal variability.

| **subseasonal sets** | **high-frequency SST (< 6 days)** | | | **low-frequency SST (6-30 days)** | | | |
|---|---|---|---|---|---|---|---|
| experiments | C–CTL | C–1day | C–3days | C–6days | C–12days | C–18days | C–30days |
| atmosphere to ocean frequency | 48/day | | | | | | |
| ocean to atmosphere Frequency | 48/day | 1/1day | 1/3days | 1/6days | 1/12days | 1/18days | 1/30days |

https://doi.org/10.5194/gmd-2023-152
Preprint. Discussion started: 30 August 2023



Table 2. The average DJF temperature difference between SST and 10m depth ($\overline{\Delta \boldsymbol{T}_{0-10m}}$) and 30m depth ($\overline{\Delta \boldsymbol{T}_{0-30m}}$), and the boreal winter phase mean of 20–100-day bandpass filter with max/mini SST and oceanic 10m depth temperature ($T_{10m}$) in the area of (110–130° E, 5–15° S), with observation (OISST), AGCM (A–CTL), high-frequency experiments (C–CTL, C–1day and C–3days) and low-frequency experiments (C–6days, C–12days, C–18days and C–30days)

| **(110–130° E, 5–15° S)** | | **obs.** | **AGCM** | **high-frequency** | | | **low-frequency** | | | |
|---|---|---|---|---|---|---|---|---|---|---|
| experiments | | OI SST[1] | A–CTL[2] | C–CTL | C–1day | C–3days | C–6days | C–12days | C–18days | C–30days |
| DJF seasonal mean | SST | 302.2 ±0.96 | 302.2 ±0.77 | 300.8 ±0.76 | 301.2 ±0.76 | 301.2 ±0.75 | 301.2 ±0.75 | 301.4 ±0.75 | 301.6 ±0.80 | 302.7 ±1.71 |
| | $\overline{\Delta T}_{0-10m}$ | - | - | 0.1 ± 0.22 | 0.1 ± 0.22 | 0.1 ± 0.21 | 0.1 ± 0.23 | 0.2 ± 0.25 | 0.3 ± 0.32 | 1.0 ± 0.95 |
| | $\overline{\Delta T}_{0-30m}$ | - | - | 0.8 ± 0.79 | 0.7 ± 0.70 | 0.6 ± 0.69 | 0.8 ± 0.70 | 0.8 ± 0.70 | 1.0 ± 0.73 | 2.1 ± 1.54 |
| phase's mean in boreal winter | max SST (phase) | 0.21 (ph2) | 0.02 (ph2) | 0.24 (ph3) | 0.26 (ph3) | 0.22 (ph3) | 0.32 (ph3) | 0.36 (ph3) | 0.43 (ph3) | 0.62 (ph2) |
| | max $T_{10m}$ (phase) | - | - | 0.15 (ph4) | 0.17 (ph4) | 0.14 (ph3) | 0.19 (ph3) | 0.21 (ph3) | 0.26 (ph3) | 0.35 (ph2) |
| | mini SST (phase) | -0.21 (ph7) | -0.003 (ph8) | -0.17 (ph7) | -0.22 (ph7) | -0.19 (ph7) | -0.25 (ph7) | -0.28 (ph7) | -0.38 (ph7) | -0.60 (ph6) |
| | mini $T_{10m}$ (phase) | - | - | -0.11 (ph8) | -0.12 (ph7) | -0.11 (ph8) | -0.15 (ph7) | -0.17 (ph7) | -0.24 (ph7) | -0.33 (ph6) |

Note: [1]daily average data, [2] monthly average data.

https://doi.org/10.5194/gmd-2023-152
Preprint. Discussion started: 30 August 2023




Table 3. The average 20–100-day filtered outgoing longwave radiation (OLR), latent heat flux (LHF), net surface solar radiation (FSNS), 850-hPa zonal wind (U850), column-integrated MSE tendency (<dmdt>), column-integrated vertical MSE advection (-<wdmdp>), and column-integrated horizontal MSE advection (-<vdm>) during the boreal winter are categorized into SST warming and SST cooling states. This categorization is performed over two domains, namely (110–130° E, 5–15° S) and (120–150° E, 0–10° S), as mentioned in the note.

| | | **obs.** | **AGCM** | **high-frequency** | | | **low-frequency** | | | |
|---|---|---|---|---|---|---|---|---|---|---|
| | experiments | ERA5/ NOAA | A– CTL | C– CTL | C– 1day | C– 3days | C– 6days | C– 12days | C– 18days | C– 30days |
| SST warming | OLR[1] | 16.3 | 6.3 | 14.8 | 16.5 | 16.0 | 18.5 | 19.5 | 19.3 | 11.1 |
| | (phase) | (ph1) | (ph2) | (ph2) | (ph2) | (ph2) | (ph2) | (ph1) | (ph1) | (ph8) |
| | LHF[1] | -10.1 | -11.1 | -7.3 | -7.3 | -6.0 | -8.6 | -11.3 | -19.3 | -21.9 |
| | (phase) | (ph3) | (ph3) | (ph3) | (ph3) | (ph2) | (ph2) | (ph3) | (ph2) | (ph1) |
| | FSNS[1] | -15.7 | -8.9 | -15.7 | -17.9 | -15.9 | -19.5 | -18.6 | -16.8 | -9.5 |
| | (phase) | (ph1) | (ph2) | (ph2) | (ph2) | (ph2) | (ph2) | (ph1) | (ph2) | (ph1) |
| | U850[1] | -3.0 | -2.3 | -3.0 | -2.8 | -2.3 | -2.9 | -2.8 | -3.4 | -2.2 |
| | (phase) | (ph2) | (ph3) | (ph3) | (ph3) | (ph3) | (ph3) | (ph3) | (ph2) | (ph2) |
| | <dmdt>[2] | 10.7 | 9.1 | 8.2 | 8.2 | 5.6 | 7.9 | 8.1 | 7.0 | 4.1 |
| | (phase) | (ph3) | (ph3) | (ph3) | (ph3) | (ph3) | (ph3) | (ph2) | (ph2) | (ph3) |
| | -<wdmdp>[2] | 18.2 | 8.4 | 12.9 | 19.2 | 13.9 | 17.9 | 18.1 | 21.9 | 10.4 |
| | (phase) | (ph1) | (ph2) | (ph1) | (ph1) | (ph1) | (ph1) | (ph1) | (ph1) | (ph1) |
| | -<vdm>[2] | 11.5 | 5.3 | 7.9 | 7.9 | 4.4 | 8.4 | 9.0 | 9.1 | 14.0 |
| | (phase) | (ph2) | (ph3) | (ph3) | (ph3) | (ph3) | (ph3) | (ph3) | (ph2) | (ph1) |
| SST cooling | OLR[1] | -19.2 | -8.9 | -11.3 | -14.2 | -15.0 | -20.9 | -20.3 | -22.5 | -11.0 |
| | (phase) | (ph5) | (ph6) | (ph6) | (ph6) | (ph6) | (ph5) | (ph5) | (ph5) | (ph5) |
| | LHF[1] | 15.6 | 17.3 | 7.4 | 8.0 | 7.0 | 8.7 | 15.2 | 18.1 | 29.8 |
| | (phase) | (ph6) | (ph7) | (ph7) | (ph6) | (ph6) | (ph6) | (ph6) | (ph6) | (ph6) |
| | FSNS[1] | 19.7 | 10.5 | 11.6 | 16.6 | 16.1 | 21.9 | 19.1 | 21.6 | 10.4 |
| | (phase) | (ph5) | (ph5) | (ph6) | (ph6) | (ph6) | (ph5) | (ph5) | (ph5) | (ph5) |
| | U850[1] | 3.5 | 2.6 | 2.6 | 2.7 | 2.3 | 2.8 | 2.8 | 3.4 | 2.7 |
| | (phase) | (ph6) | (ph6) | (ph7) | (ph6) | (ph7) | (ph7) | (ph6) | (ph6) | (ph6) |
| | <dmdt>[2] | -10.6 | -7.5 | -9.0 | -7.9 | -6.0 | -9.0 | -8.2 | -8.9 | -3.8 |
| | (phase) | (ph6) | (ph7) | (ph7) | (ph6) | (ph6) | (ph6) | (ph6) | (ph6) | (ph7) |
| | -<wdmdp>[2] | -23.6 | -9.3 | -12.6 | -12.8 | -15.1 | -19.3 | -19.5 | -24.5 | -16.9 |
| | (phase) | (ph5) | (ph6) | (ph6) | (ph6) | (ph5) | (ph5) | (ph5) | (ph5) | (ph5) |
| | -<vdm>[2] | -12.5 | -7.0 | -8.6 | -7.6 | -5.9 | -7.0 | -8.5 | -11.3 | -17.9 |
| | (phase) | (ph7) | (ph7) | (ph7) | (ph7) | (ph7) | (ph7) | (ph6) | (ph6) | (ph5) |

Note: [1] domain (110–130° E, 5–15° S) refer to Table 2 and Fig. 9, and [2] domain (120–150° E, 0–10° S) refer to Fig. 11.

https://doi.org/10.5194/gmd-2023-152
Preprint. Discussion started: 30 August 2023



**Figure List**

**Figure 1.** Wavenumber–frequency spectra for 850-hPa zonal wind averaged over 10° S–10° N in boreal winter after removing the climatological mean seasonal cycle. Vertical dashed lines represent periods at 80 and 30 days, respectively. (a)–(i) are from ERA5 reanalysis, A–CTL, C–CTL, C–1day, C–3days, C–6days, C–12days, C–18days, and C–30days, respectively.

**Figure 2.** Hovmöller diagrams of the correlation between the precipitation averaged over 10° S–5° N, 75–100° E and the intraseasonally filtered precipitation (color) and 850-hPa zonal wind (contour) averaged over 10° N–10° S. (a)–(i) arrange in order are same as Fig. 1 from GPCP/ERA5 and all experiments.

**Figure 3.** Zonal wavenumber–frequency power spectra of anomalous OLR (colors) and phase lag with U850 (vectors) for the symmetric component of tropical waves, with the vertically upward vector representing a phase lag of 0° with phase lag increasing clockwise. Three dispersion straight lines with increasing slopes represent the equatorial Kelvin waves (derived from the shallow water equations) corresponding to three equivalent depths, 12, 25, and 50 m, respectively. (a)–(i) arrange in order are same as Fig. 1 from NOAA/ERA5 and all experiments.

**Figure 4.** Phase-longitude Hovmöller diagrams of 20–100-day filtered precipitation (mm day$^{-1}$, shaded) and SST anomaly (K, contour) averaged over 10° N–10° S from phase 1 to 8. Contour interval is 0.03; solid, dashed, and thick-black lines represent positive, negative, and zero values, respectively. (a)–(i) arrange in order are same as Fig. 1 from GPCP/OISST and all experiments.

**Figure 5.** Phase-vertical Hovmöller diagrams of 20–100-day specific humidity (shading, g kg$^{-1}$) and air temperture (contoured, K) averaged over 10° N–10° S, 120–150° E; solid, dashed, and thick-black curves are positive, negative, and zero values, respectively. (a)–(i) arrange in order are same as Fig. 1 from ERA5 and all experiments.

**Figure 6.** 15° N–15° S averaged p-vertical velocity anomaly (Pa s$^{-1}$, shaded) and zonal wind anomaly (m s$^{-1}$, contour, interval 0.5) between phase 3 and phase 4; solid, dashed, and thick-black lines represent positive, negative, and zero values, respectively.

https://doi.org/10.5194/gmd-2023-152
Preprint. Discussion started: 30 August 2023




**Figure 7.** The average 20–100-day filtered oceanic temperature (K, shaded and contour, interval 0.03) between 0 and 60 m depth for MJO phase 2–3. (a)–(g) are from C–CTL, C–1day, C–3days, C–6days, C–12days, C–18days, and C–30days, respectively.

**Figure 8.** The near-equatorial RMM1 and RMM2 variances in a bar graph based on Wheeler and Hendon (2004) with observation and reanalysis data (NOAA/ERA5), AGCM (A–CTL), high-frequency experiments (C–CTL, C–1day and C–3days) and low-frequency experiments (C–6days, C–12days, C–18days and C–30days).

**Figure 9.** The lead-lag relationship between MJO-related atmosphere and sub-seasonal SST variation is examined between phase 1 and 8 within the domain of 110–130° E and 5–15° S. The variables analyzed include 20-100-day filtered latent heat flux (LHF, represented by green shading), outgoing longwave radiation (OLR, represented by yellow bar chart), net surface solar radiation (FSNS, represented by orange bar chart), 850-hPa zonal wind (U850, represented by purple bar chart), 30-m depth oceanic temperature (30-m T multiplied by 100, represented by black line), and sea surface temperatures (SST multiplied by 10, represented by orange line). The graphic expression of variables denoted with (L) indicates the use of the left y-axis, while variables denoted with (R) use the right y-axis. (a)–(i) are from ERA5/OISST reanalysis, A–CTL, C–CTL, C–1day, C–3days, C–6days, C–12days, C–18days, and C–30days, respectively.

**Figure 10.** Phase 4 average 20–100-day filtered OLR (W m$^{-2}$, shaded) and 200 hPa zonal wind anomaly (m s$^{-1}$, vector) with the reference vector (2 m s$^{-1}$) shown at the top right of each panel at the top panel; latent heat flux (W m$^{-2}$, shaded) which positive anomaly represents upward, and 10-m wind anomaly (m s$^{-1}$, contour interval 0.2); solid, dashed, and thick-black lines represent positive, negative, and zero values, respectively, at the second panel from the top, net surface heat flux (W m$^{-2}$, shaded) and net solar radiation (W m$^{-2}$, contour interval 3) at the third panel from the top, and SST (K, shaded) and 850 hPa zonal wind anomaly (m s$^{-1}$, vector) with the reference vector (1 m s$^{-1}$) shown at the top right of each panel at the bottom panel. The number of days used to generate the composite is shown at the bottom right corner of each panel and vertical black line of each panel indicates the dateline. (a), (d), (g) and (j) are from C–CTL; (b), (e), (h) and (k) are from C–18days, and (c), (f), (i) and (l) are from C–30days, respectively.

https://doi.org/10.5194/gmd-2023-152
Preprint. Discussion started: 30 August 2023

Geoscientific Model Development
Discussions
Open Access
EGU

**Figure 11.** The bar chart illustrates anomalies in the average 20–100-day filtered column-integrated MSE budget terms (J kg$^{-1}$ s$^{-1}$) across the domain (10° S–0° N/S, 120–150° E) for REA5 and all model simulations. Different colors represent different datasets: green for REA5, light gray for A–CTL, red, orange and wathet blue for high-frequency experiments (C–CTL, C–1day, and C–3days), respectively, purple, blue, dark brown, and dark gray for low-frequency experiments (C–6days, C–12days, C–18days, and C–30days), respectively. The bars from left to right represent column-integrated MSE tendency (<dmdt>), column-integrated vertical MSE advection (-<wdmdp>), column-integrated horizontal MSE advection (-<vdm>), surface latent heat fluxes (LH), surface sensible heat fluxes (SH), shortwave radiation fluxes (<SW>), longwave radiation fluxes (<LW>) and residual terms, respectively.

**Figure 12.** Phase 5 anomalies of 20–100-day filtered the column-integrated MSE tendency (J kg$^{-1}$ s$^{-1}$, shading), precipitation (mm d$^{-1}$, contours interval 1.0) and 850-hPa wind (green vector) with the reference vector (2 m s$^{-1}$) based on (a) ERA5, (b) A−CTL, (c) C−CTL, (d) C−1day, (e) C−3days, (f) C−6days, (g) C−12days, (h) C−18days and (i) C−30days. The solid-red, dashed-blue, and thick-black curves represent positive, negative, and zero values, respectively. The vertical black line in each panel indicates the dateline.

**Figure 13.** (a) The relative role of each MSE component of phase 5 through the projection of the spatial pattern of each MSE budget over the MC (20° S–20° N, 90–210° E) onto the total MSE tendency pattern (Fig. 12a). (b–c) Decomposite of the total horizontal MSE advection based on zonal and meridional components of high-frequency SST feedback experiments (C–CTL, A–CTL, C–1day and C–3days) and low-frequency SST feedback experiments (C–6days, C–12days, C–18days and C–30days), respectively.

**Figure 14.** Phase 5 anomalies of 20–100-day filtered the column-integrated vertical MSE advection (J kg$^{-1}$ s$^{-1}$, shading), column-integrated horizontal MSE advection (J kg$^{-1}$ s$^{-1}$, contours interval 6.0) and 200-hPa wind (green vector) with the reference vector (3 m s$^{-1}$) based on (a) ERA5, (b) A−CTL, (c) C−CTL, (d) C−1day, (e) C−3days, (f) C−6days, (g) C−12days, (h) C−18days and (i) C−30days. The solid-blue, dashed-red, and thick-black curves represent positive, negative, and zero values, respectively. The vertical black line in each panel indicates the dateline.

**Figure 15.** The sketch map illustrates the equatorial circulation anomalies and moistening processes during the eastward propagation of the MJO in boreal winter for

https://doi.org/10.5194/gmd-2023-152
Preprint. Discussion started: 30 August 2023



various experiments: (a) uncoupled A−CTL, (b) high-frequency SST feedback experiments (C−CTL, C−1day, and C−3days), (c) low-frequency SST feedback experiments (C−6days, C−12days, and C−18days), and (d) C−30days experiment. In each panel, the horizontal line represents the equator. The clustering of gray clouds (size) indicates the strength of convective organization. A red ellipse indicates conventionally driven circulation anomalies. In the coupled simulations, light red (blue) filled ovals represent warm (cold) SST anomalies (SSTA), and a grass green filled rectangle represents latent heat flux anomalies. Unresolved convective processes are indicated by black dots representing low-level moisture. Low-level moisture convergence into the equatorial trough is shown by light blue arrows, while midlevel moisture advection is represented by left-pointing green arrows. The deeper colors or thicker lines on the map indicate stronger anomalies of the MJO factors. Note: The concept of the figure is based on DeMott et al. (2014), as depicted in Fig. 11.

https://doi.org/10.5194/gmd-2023-152
Preprint. Discussion started: 30 August 2023


Geoscientific Model Development
Discussions
Open Access
EGU

1296 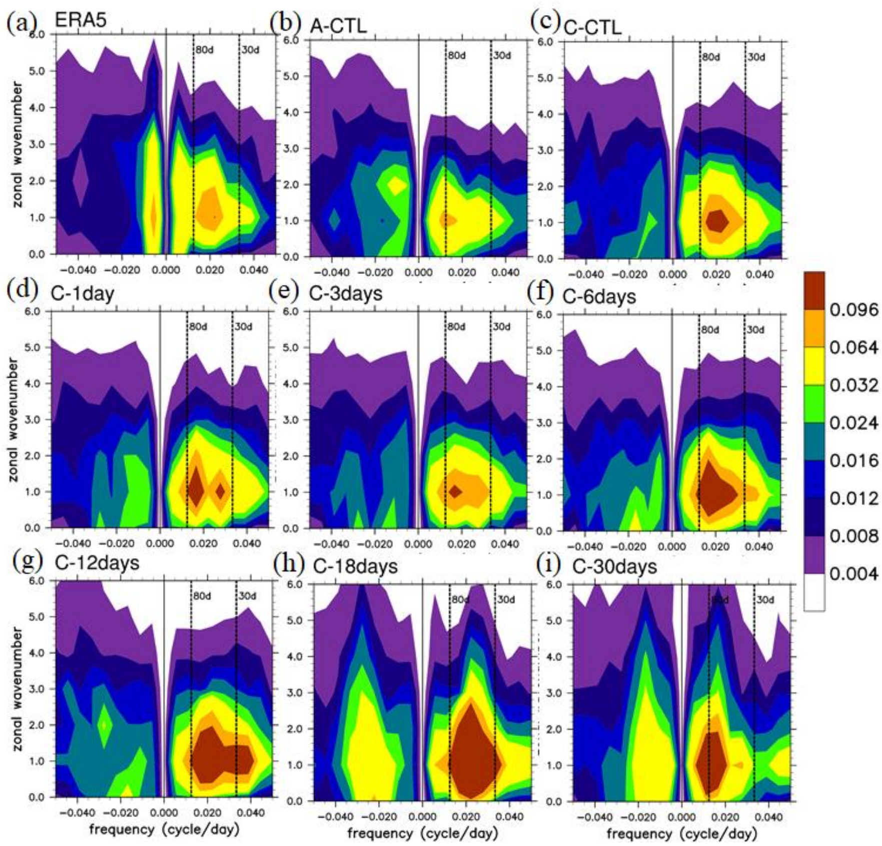


1297 **Figure 1.** Wavenumber–frequency spectra for 850-hPa zonal wind averaged over 10°
1298 S–10° N in boreal winter after removing the climatological mean seasonal cycle.
1299 Vertical dashed lines represent periods at 80 and 30 days, respectively. (a)–(i) are
1300 from ERA5 reanalysis, A–CTL, C–CTL, C–1day, C–3days, C–6days, C–12days, C–
1301 18days, and C–30days, respectively.

https://doi.org/10.5194/gmd-2023-152
Preprint. Discussion started: 30 August 2023



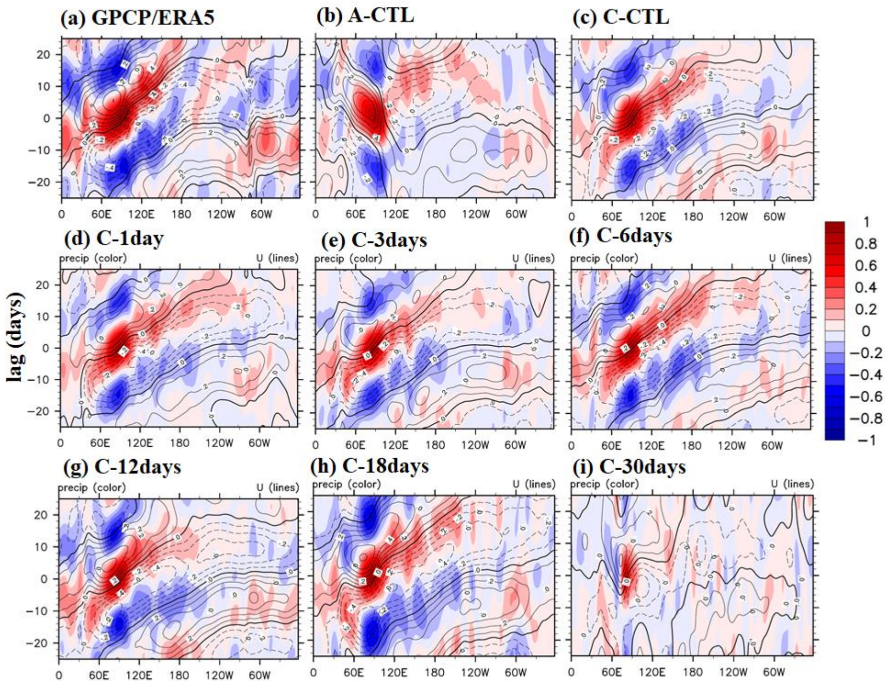


**Figure 2.** Hovmöller diagrams of the correlation between the precipitation averaged over 10° S–5° N, 75–100° E and the intraseasonally filtered precipitation (color) and 850-hPa zonal wind (contour) averaged over 10° N–10° S. (a)–(i) arrange in order are same as Fig. 1 from GPCP/ERA5 and all experiments.

https://doi.org/10.5194/gmd-2023-152
Preprint. Discussion started: 30 August 2023


Geoscientific Model Development
Discussions
Open Access

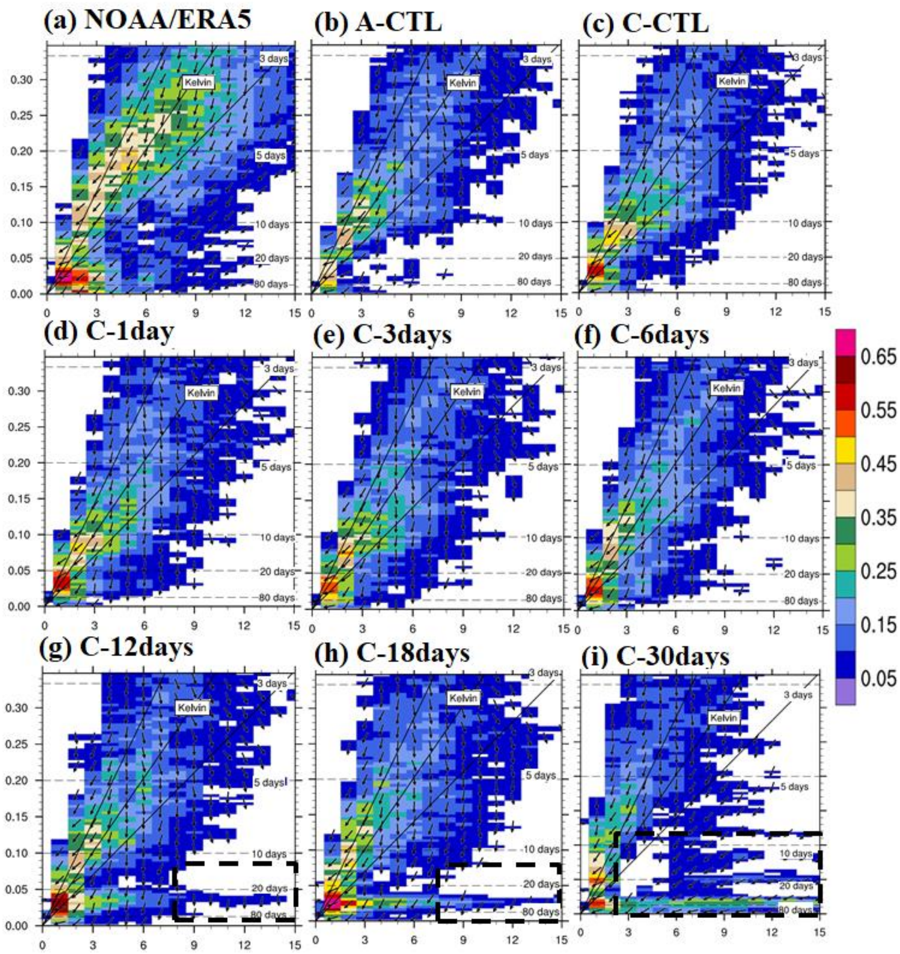


**Figure 3.** Zonal wavenumber–frequency power spectra of anomalous OLR (colors) and phase lag with U850 (vectors) for the symmetric component of tropical waves, with the vertically upward vector representing a phase lag of 0° with phase lag increasing clockwise. Three dispersion straight lines with increasing slopes represent the equatorial Kelvin waves (derived from the shallow water equations) corresponding to three equivalent depths, 12, 25, and 50 m, respectively. (a)–(i) arrange in order are same as Fig. 1 from NOAA/ERA5 and all experiments.

https://doi.org/10.5194/gmd-2023-152
Preprint. Discussion started: 30 August 2023

Geoscientific Model Development
Discussions
Open Access

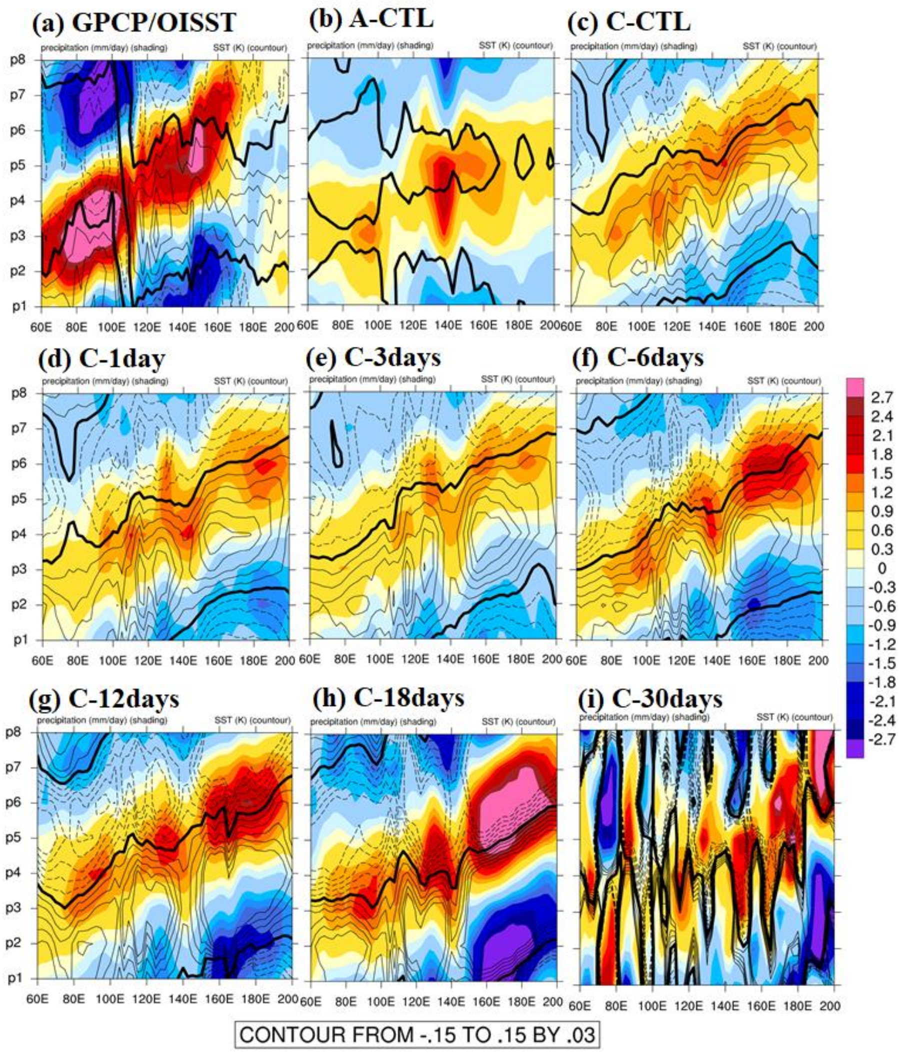


**Figure 4.** Phase-longitude Hovmöller diagrams of 20–100-day filtered precipitation (mm day$^{-1}$, shaded) and SST anomaly (K, contour) averaged over 10° N–10° S from phase 1 to 8. Contour interval is 0.03; solid, dashed, and thick-black lines represent positive, negative, and zero values, respectively. (a)–(i) arrange in order are same as Fig. 1 from GPCP/OISST and all experiments.

https://doi.org/10.5194/gmd-2023-152
Preprint. Discussion started: 30 August 2023



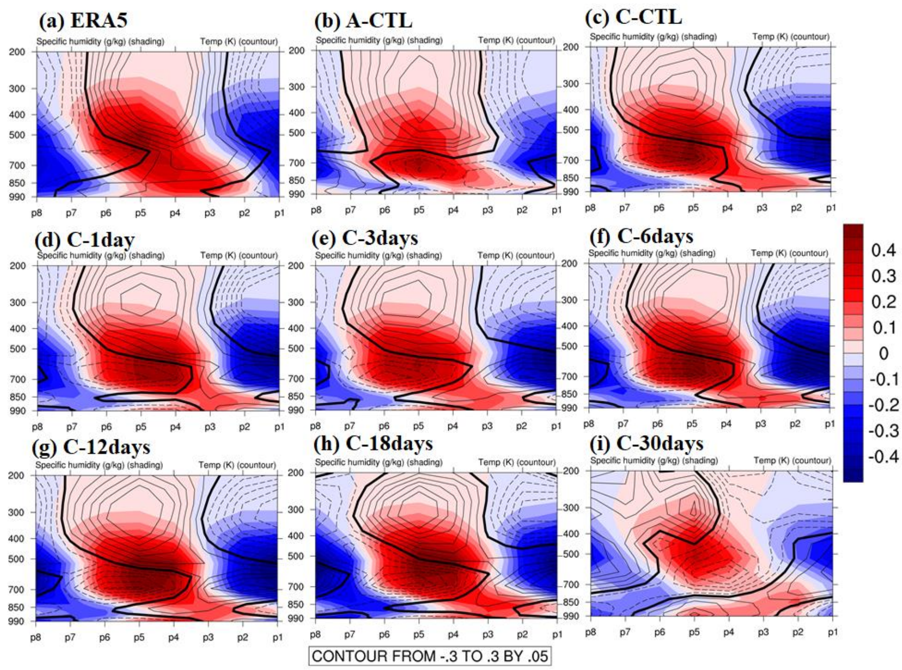


**Figure 5.** Phase-vertical Hovmöller diagrams of 20–100-day specific humidity (shading, g kg$^{-1}$) and air temperture (contoured, K) averaged over 10° N–10° S, 120–150° E; solid, dashed, and thick-black curves are positive, negative, and zero values, respectively. (a)–(i) arrange in order are same as Fig. 1 from ERA5 and all experiments.

https://doi.org/10.5194/gmd-2023-152
Preprint. Discussion started: 30 August 2023

Geoscientific Model Development
Discussions

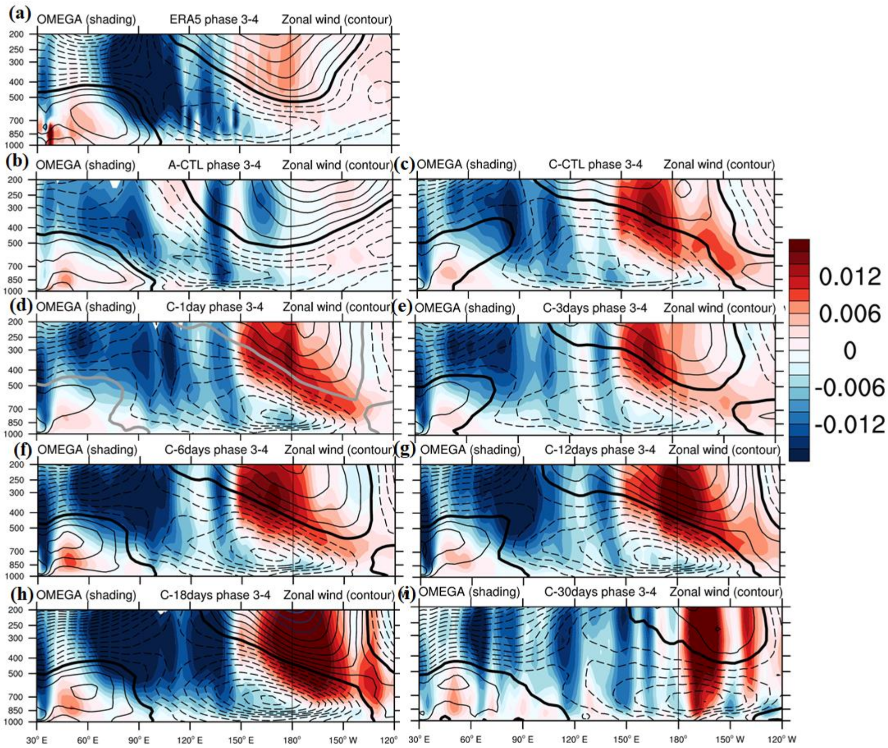


**Figure 6.** 15° N–15° S averaged p-vertical velocity anomaly (Pa s$^{-1}$, shaded) and zonal wind anomaly (m s$^{-1}$, contour, interval 0.5) between phase 3 and phase 4; solid, dashed, and thick-black lines represent positive, negative, and zero values, respectively.

https://doi.org/10.5194/gmd-2023-152
Preprint. Discussion started: 30 August 2023



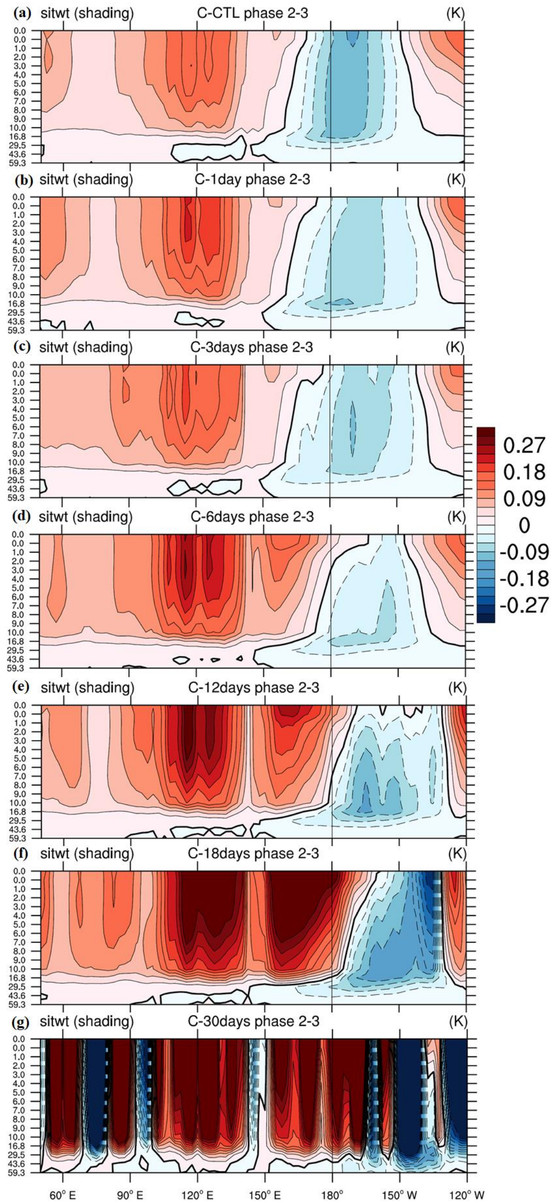


**Figure 7.** The average 20–100-day filtered oceanic temperature (K, shaded and contour, interval 0.03) between 0 and 60 m depth for MJO phase 2–3. (a)–(g) are from C–CTL, C–1day, C–3days, C–6days, C–12days, C–18days, and C–30days, respectively.

https://doi.org/10.5194/gmd-2023-152
Preprint. Discussion started: 30 August 2023

Geoscientific Model Development
Discussions
Open Access

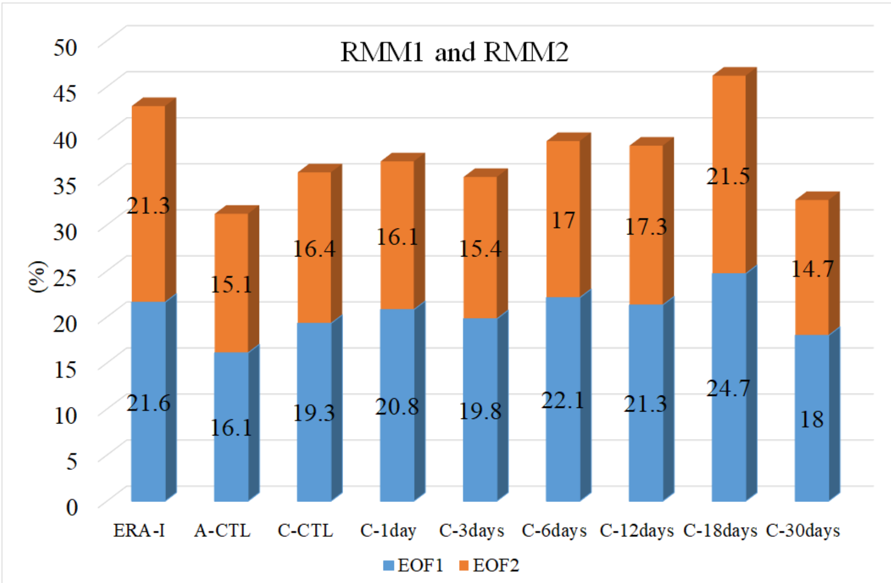


**Figure 8.** The near-equatorial RMM1 and RMM2 variances in a bar graph based on Wheeler and Hendon (2004) with observation and reanalysis data (NOAA/ERA5), AGCM (A–CTL), high-frequency experiments (C–CTL, C–1day and C–3days) and low-frequency experiments (C–6days, C–12days, C–18days and C–30days).

https://doi.org/10.5194/gmd-2023-152
Preprint. Discussion started: 30 August 2023


Geoscientific Model Development
Discussions
Open Access

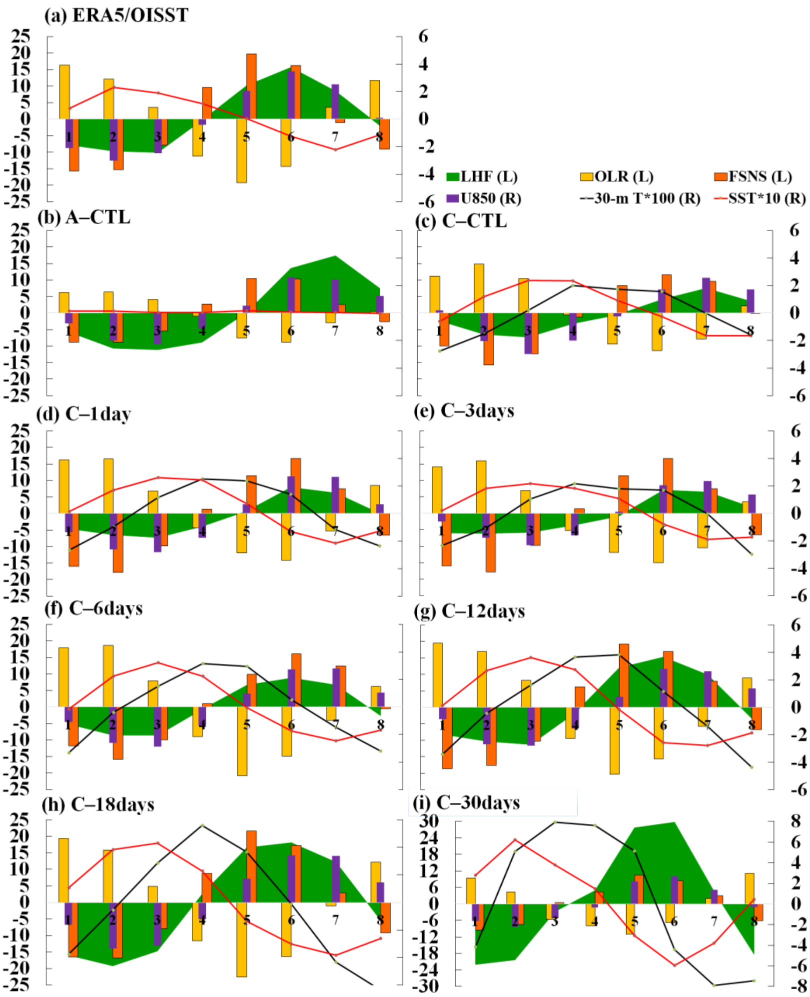


**Figure 9.** The lead-lag relationship between MJO-related atmosphere and sub-seasonal SST variation is examined between phase 1 and 8 within the domain of 110–130° E and 5–15° S. The variables analyzed include 20-100-day filtered latent heat flux (LHF, represented by green shading), outgoing longwave radiation (OLR, represented by yellow bar chart), net surface solar radiation (FSNS, represented by orange bar chart), 850-hPa zonal wind (U850, represented by purple bar chart), 30-m depth oceanic temperature (30-m T multiplied by 100, represented by black line), and sea surface temperatures (SST multiplied by 10, represented by orange line). The graphic expression of variables denoted with (L) indicates the use of the left y-axis, while variables denoted with (R) use the right y-axis. (a)–(i) are from ERA5/OISST reanalysis, A–CTL, C–CTL, C–1day, C–3days, C–6days, C–12days, C–18days, and C–30days, respectively.

https://doi.org/10.5194/gmd-2023-152
Preprint. Discussion started: 30 August 2023




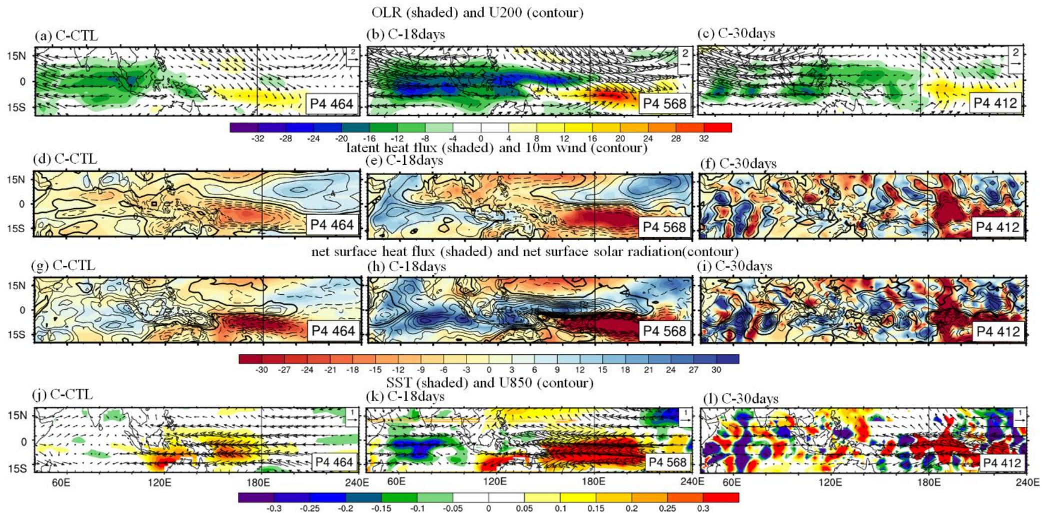


**Figure 10.** Phase 4 average 20–100-day filtered OLR (W m$^{-2}$, shaded) and 200 hPa zonal wind anomaly (m s$^{-1}$, vector) with the reference vector (2 m s$^{-1}$) shown at the top right of each panel at the top panel; latent heat flux (W m$^{-2}$, shaded) which positive anomaly represents upward, and 10-m wind anomaly (m s$^{-1}$, contour interval 0.2); solid, dashed, and thick-black lines represent positive, negative, and zero values, respectively, at the second panel from the top, net surface heat flux (W m$^{-2}$, shaded) and net solar radiation (W m$^{-2}$, contour interval 3) at the third panel from the top, and SST (K, shaded) and 850 hPa zonal wind anomaly (m s$^{-1}$, vector) with the reference vector (1 m s$^{-1}$) shown at the top right of each panel at the bottom panel. The number of days used to generate the composite is shown at the bottom right corner of each panel and vertical black line of each panel indicates the dateline. (a), (d), (g) and (j) are from C–CTL; (b), (e), (h) and (k) are from C–18days, and (c), (f), (i) and (l) are from C–30days, respectively.

https://doi.org/10.5194/gmd-2023-152
Preprint. Discussion started: 30 August 2023


Geoscientific Model Development
Discussions

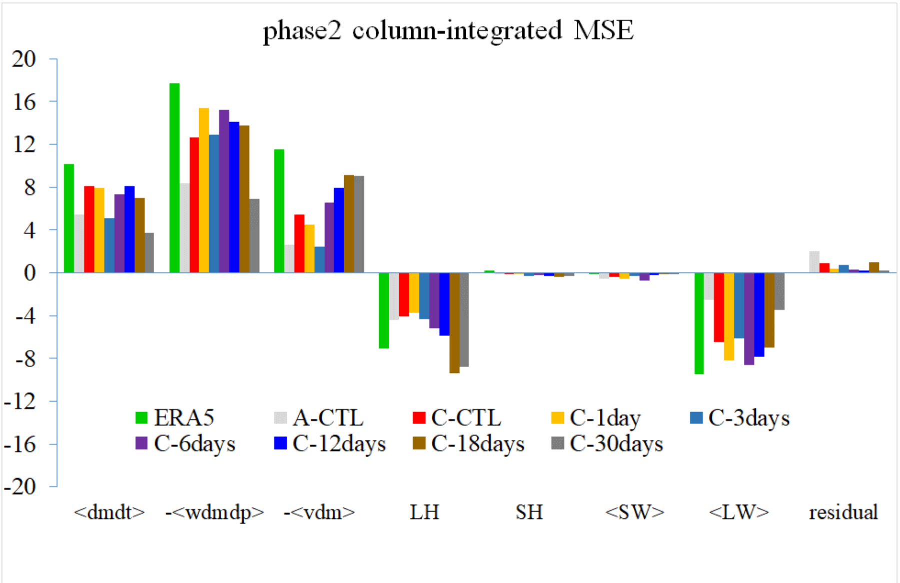


**Figure 11.** The bar chart illustrates anomalies in the average 20–100-day filtered column-integrated MSE budget terms (J kg$^{-1}$ s$^{-1}$) across the domain (10° S–0° N/S, 120–150° E) for REA5 and all model simulations. Different colors represent different datasets: green for REA5, light gray for A–CTL, red, orange and wathet blue for high-frequency experiments (C–CTL, C–1day, and C–3days), respectively, purple, blue, dark brown, and dark gray for low-frequency experiments (C–6days, C–12days, C–18days, and C–30days), respectively. The bars from left to right represent column-integrated MSE tendency (<dmdt>), column-integrated vertical MSE advection (-<wdmdp>), column-integrated horizontal MSE advection (-<vdm>), surface latent heat fluxes (LH), surface sensible heat fluxes (SH), shortwave radiation fluxes (<SW>), longwave radiation fluxes (<LW>) and residual terms, respectively.

https://doi.org/10.5194/gmd-2023-152
Preprint. Discussion started: 30 August 2023


Geoscientific Model Development
Discussions
Open Access

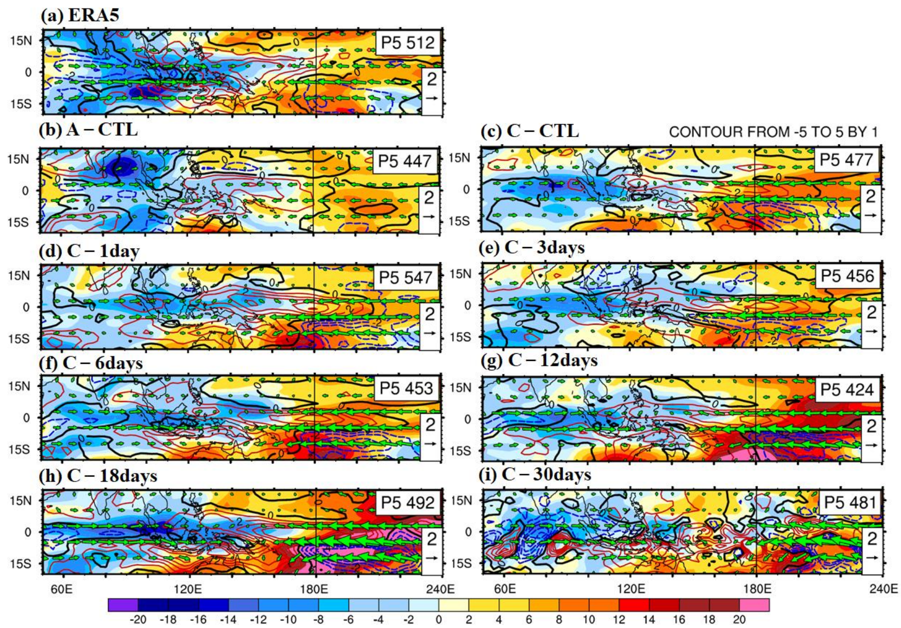


**Figure 12.** Phase 5 anomalies of 20–100-day filtered the column-integrated MSE tendency (J kg$^{-1}$ s$^{-1}$, shading), precipitation (mm d$^{-1}$, contours interval 1.0) and 850-hPa wind (green vector) with the reference vector (2 m s$^{-1}$) based on (a) ERA5, (b) A−CTL, (c) C−CTL, (d) C−1day, (e) C−3days, (f) C−6days, (g) C−12days, (h) C−18days and (i) C−30days. The solid-red, dashed-blue, and thick-black curves represent positive, negative, and zero values, respectively. The vertical black line in each panel indicates the dateline.

https://doi.org/10.5194/gmd-2023-152
Preprint. Discussion started: 30 August 2023

Geoscientific Model Development
Open Access
Discussions

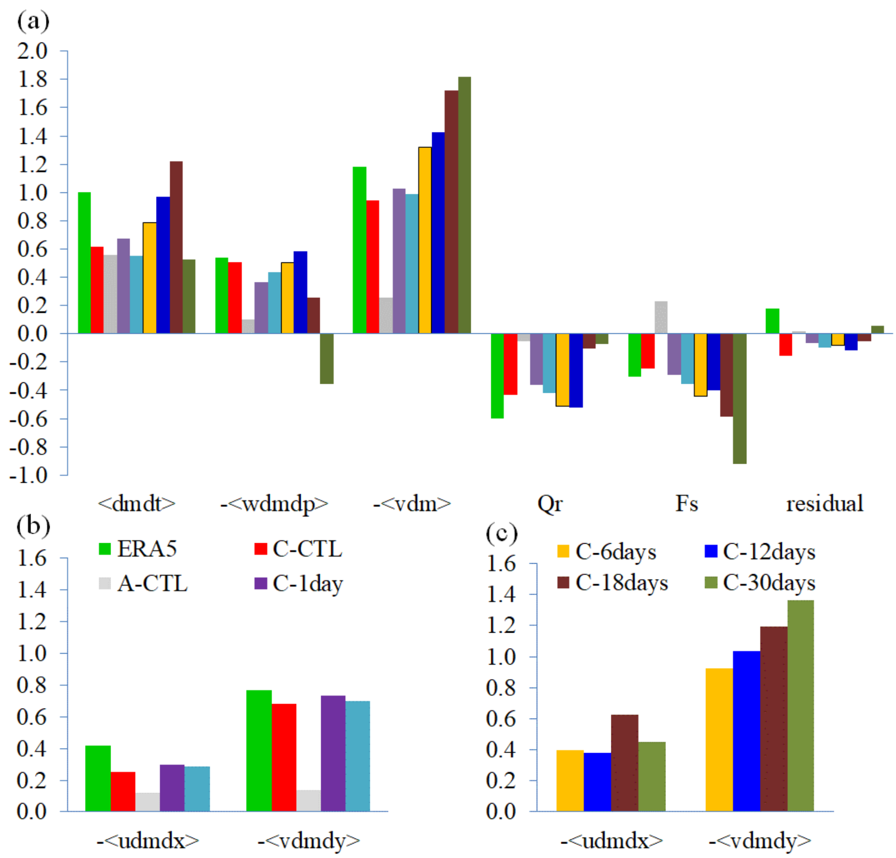


1389

1390 **Figure 13.** (a) The relative role of each MSE component of phase 5 through the
1391 projection of the spatial pattern of each MSE budget over the MC (20° S–20° N, 90–
1392 210° E) onto the total MSE tendency pattern (Fig. 12a). (b–c) Decomposite of the total
1393 horizontal MSE advection based on zonal and meridional components of high-
1394 frequency SST feedback experiments (C–CTL, A–CTL, C–1day and C–3days) and
1395 low-frequency SST feedback experiments (C–6days, C–12days, C–18days and C–
1396 30days), respectively.

https://doi.org/10.5194/gmd-2023-152
Preprint. Discussion started: 30 August 2023


Geoscientific Model Development
Open Access
Discussions

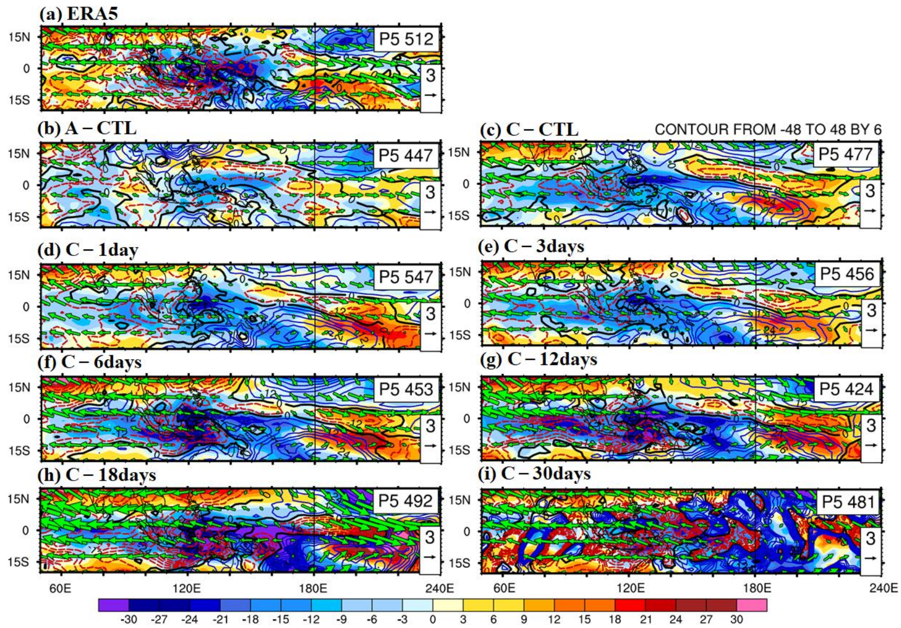


**Figure 14.** Phase 5 anomalies of 20–100-day filtered the column-integrated vertical MSE advection (J kg$^{-1}$ s$^{-1}$, shading), column-integrated horizontal MSE advection (J kg$^{-1}$ s$^{-1}$, contours interval 6.0) and 200-hPa wind (green vector) with the reference vector (3 m s$^{-1}$) based on (a) ERA5, (b) A−CTL, (c) C−CTL, (d) C−1day, (e) C−3days, (f) C−6days, (g) C−12days, (h) C−18days and (i) C−30days. The solid-blue, dashed-red, and thick-black curves represent positive, negative, and zero values, respectively. The vertical black line in each panel indicates the dateline.

https://doi.org/10.5194/gmd-2023-152
Preprint. Discussion started: 30 August 2023

Geoscientific Model Development
Discussions

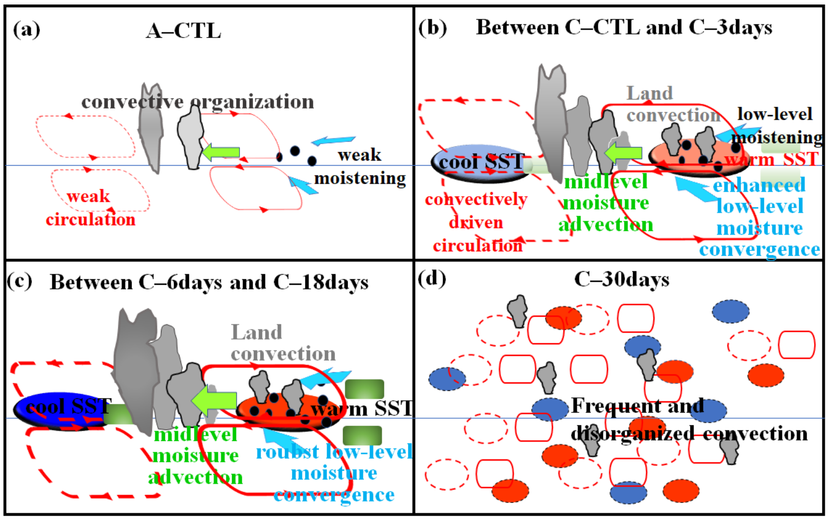


**Figure 15.** The sketch map illustrates the equatorial circulation anomalies and moistening processes during the eastward propagation of the MJO in boreal winter for various experiments: (a) uncoupled A−CTL, (b) high-frequency SST feedback experiments (C−CTL, C−1day, and C−3days), (c) low-frequency SST feedback experiments (C−6days, C−12days, and C−18days), and (d) C−30days experiment. In each panel, the horizontal line represents the equator. The clustering of gray clouds (size) indicates the strength of convective organization. A red ellipse indicates conventionally driven circulation anomalies. In the coupled simulations, light red (blue) filled ovals represent warm (cold) SST anomalies, and a grass green filled rectangle represents latent heat flux anomalies. Unresolved convective processes are indicated by black dots representing low-level moisture. Low-level moisture convergence into the equatorial trough is shown by light blue arrows, while midlevel moisture advection is represented by left-pointing green arrows. The deeper colors or thicker lines on the map indicate stronger anomalies of the MJO factors. Note: The concept of the figure is based on DeMott et al. (2014), as depicted in Fig. 11.